Optical Coherence Tomography: System Design and Noise Analysis

Frosz, Michael H.; Juhl, Michael; Lang, Morten H.

Publication date:
2001

Document Version
Publisher's PDF, also known as Version of record

Risø-R-1278(EN)

Optical Coherence Tomography: System Design and Noise Analysis

Michael H. Frosz
Michael Juhl
Morten H. Lang

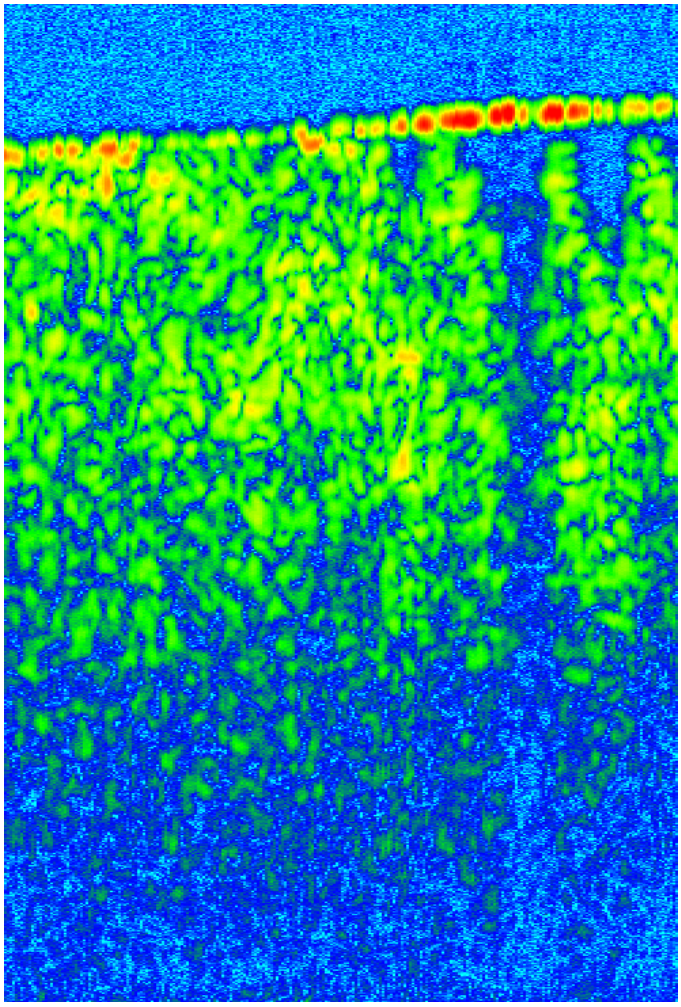

Risø National Laboratory, Roskilde, Denmark
July 2001

Risø–R–1278(EN)

Optical Coherence Tomography: System Design and Noise Analysis

Michael H. Frosz c973841
Michael Juhl c973750
Morten H. Lang c973868

Risø National Laboratory, Roskilde, Denmark
July 2001

Abstract The basic properties of an Optical Coherence Tomography (OCT) system, such as coherence and interference are presented. A $1.3\mu m$ light source and a $1.5\mu m$ source is examined and used in OCT imaging for comparison of penetration depth. No improvement was shown with the $1.5\mu m$ system, but is expected theoretically. A simple inexpensive $1.5\mu m$ source was also examined for use in OCT, and shows promising results, based on a spectral analysis. Noise in unbalanced and balanced detection is examined theoretically. The noise and SNR is measured experimentally for a given system, showing that the theoretical model does not give a good estimate. A model is therefore constructed using the experimental noise measurements, and shown to give better estimations of the SNR than the theoretical model. Using the new model, it is shown that attenuation of the reference power does not improve the SNR in the examined system when using unbalanced detection, as expected when using the theoretical model. It is also found that using a 25/75 coupler split ratio instead of 50/50 in balanced detection, should improve the SNR. A $50Hz$ noise was found to be picked up after filtering, and is shown to limit the SNR when no amplification of the measured signal is used.

This report is the result of a Midterm Project carried out as part of the Masters Degree programme in Civil Engineering at the Technical University of Denmark. The work was done at Risø National Laboratory.

ISBN 87–550–2905–1; ISBN 87–550–2904–3 (Internet)
ISSN 0106–2840

Information Service Department · Risø · 2001

Contents

1 Introduction

1.1 Motivation

A lot of efforts have been made through the last few decades to develop applications of optical technology in medicine and biology. There is a great demand for *in vivo* measurement technologies, which are capable of making reproducible measurements. One of these technologies is the Optical Coherence Tomography technique (OCT) [1]. OCT performs high resolution imaging of the internal microstructure in highly scattering media, e.g. biological tissue. This is done by measuring the time delay and magnitude of optical echoes at different transverse positions. The OCT technique is a spin-off from the telecommunications industry, where Optical Time Domain Reflectometry (OTDR) is used to determine the location of defects in optical fibres. However, scientists soon realized that the technique could be transferred with great advantage to medical and biological purposes. OCT systems have an advantage over competing *in vivo* techniques, such as high frequency ultra sound systems, since it offers a higher resolution. The main application is the medical field, especially ophthalmology and dermatology. The precise imaging technology is a strong tool in diagnosing eye diseases. With the OCT system it is possible to scan the retina in the back of the eye for defects to find the location and the reason to the problem. Diagnosing the eye disease glaucoma have improved greatly with OCT, since the eye disease can be diagnosed in a much earlier stage. In this field it is of course necessary to make the measurements *in vivo*, otherwise the patient would loose the ability to see. Hence, great efforts are made to develop the OCT technique to become a reliable tool in ophthalmology. Diagnosing skin cancer is another prosperous application. In contradiction to taking a biopsy, it is possible to take a great number of measurements quickly, without causing the patient any pain and without the risk of spreading the possible cancer. In these applications it is important to have as clear and detailed images as possible. Therefore, there is a good motivation to investigate the noise in the OCT system.

1.2 Project aim

The first goal of the project is to understand the basic physics and principles behind the OCT technique, so that an OCT system can be constructed in a lab. Amongst these physical phenomenons central to the OCT system is coherence and interference. To build the system, the use of different fiber-optical components, such as fiber-couplers and collimators, must be understood. The design of the system is very important, when the operational system is to be employed in an actual measurement. Thus several designs will be investigated in the course of the project.

The source of the low-coherent light used in an OCT system, is one of the basic components. The choice of this component is also of crucial importance in the imaging of a sample, since the spectral characteristics of the source used is directly related to the quality of the finished image. This motivates an examination of several sources to detemine the correlation between the source and the imaging capabilities of the OCT system.

When a biological sample is imaged with the OCT system, the purpose of the image is generally to give as accurate a description of the sample as possible. The noise is a key parameter in achieving high resolution and large penetration depth. The noise will be examined by two parallel methods: a theoretical model and an experimental determination of the noise. These two approaches will be compared

and used for an analysis of the signal to noise ratio (SNR). The SNR gives a measure of the contrast attainable with a given system.

Finally the operational OCT system will be used to image actual biological samples. Images will be recorded with different sources and different system designs to examine the influence of the system on the finished results.

The imaging of real biological samples in conjunction with the theoretical models of the system will give a valuable insight into the intricacies of a working OCT system.

1.3 Organization of this report

In this section the motivation for the work in optical coherence tomography is described as well as the goal of this specific project. In section 2 the fundamentals of a simple OCT system are presented. Important concepts such as coherence and interference are examined, and coherence lengths and spectral linewidths are defined.

The 3rd section contains a detailed analysis of the noise components expected to be found in an OCT system. A definition of the SNR is discussed and the noise terms are grouped into receiver noise, photon shot noise, excess intensity and beat noise. The reasoning behind balanced detection is verified and the noise inherent in balanced and unbalanced system designs are derived.

Section 4 contains the description of the CW sources used. The section begins with an overview of the available sources for OCT imaging and concludes with measurements of the spectrum of the sources used during the project.

In the 5th section the main results of the project is presented. The experimental setup is described in detail followed by an analysis of the noise spectrum. The next subsections present the methods used to measure the noise, followed by an explanation of the noise modeling. These preparations lead to the actual measurements of the noise. The discussion of the measured noise is supported by and compared to the theoretical models developed in section 3. This discussion is partitioned into sections concentrating on the noise in balanced/unbalanced systems and sections on splitting ratios, reflective constants and mean photocurrents.

Section 5.3 contains imaging of biological tissue, where biopsies of mice, human arteries and an onion are discussed. The biopsies are imaged with two different sources to compare these in practice. Finally the conclusion and acknowledgement follows.

2 Properties of an OCT system

The OCT in its most basic configuration consists of a simple Michelson interferometer realizable in both a bulk optic or fiber optic version. The type used here is the fiber optic one and can be seen in figure 1.

An OCT-system uses a broadband source, where the light is split in a fiber-coupler. One part of the light is directed at a reference mirror and the other part at the sample being measured. The light reflected back from the sample and reference then passes through the beam-splitter again and is collected by a detector.

Since the OCT-system is based on coherence measurements, signals are only detected when the optical path length in the sample and reference arm are within the coherence length of the source, so that if a difference in the refractive index in the sample causes light to be reflected, the detector will see an interference signal.

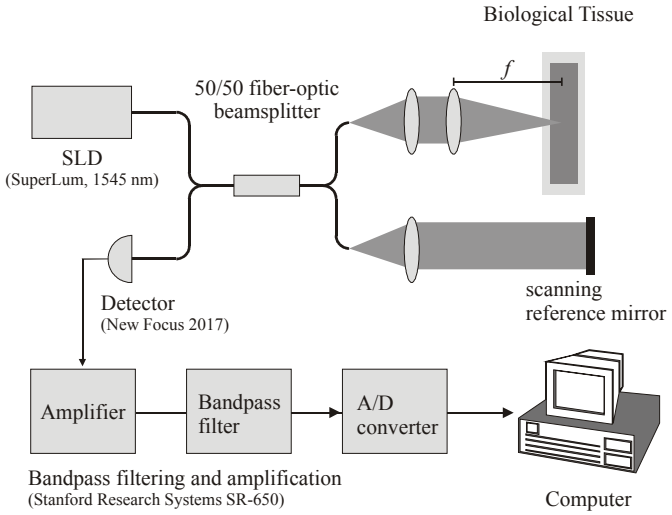

Figure 1. A diagram of a simple OCT system is shown, with the basic components. f is the focal distance of the sample lens. (Reproduced with permission from Peter E. Andersen).

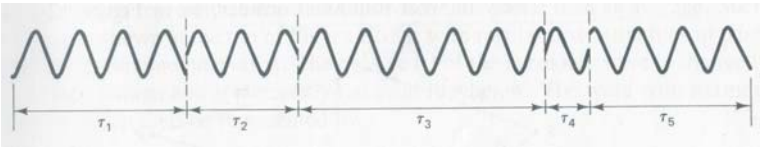

Figure 2. A sequence of wavetrains with different lifetimes τ. The average lifetime is called the coherence time τ_0. From [2].

That a difference in refractive index will cause light to be reflected was described by Fresnel, and is for normal incidence governed by the equation [2]

$$R = \left(\frac{n_1 - n_2}{n_1 + n_2}\right)^2$$

where n_1 and n_2 are the refractive indices of the media and R is the reflectivity. Setting $n_1 = 1$ (air) and $n_2 = 1.55$ (glass) this gives a reflectivity of 5%.

Moving the fiber over the sample in the two transverse directions can be used to produce a 3D image with a penetration depth of around 2-3mm in highly scattering media with a spatial resolution of 10-20μm [1].

2.1 Coherence

We now examine the coherence properties of light. For this purpose we consider light as electromagnetic radiation, which can be described as [2]

$$\mathbf{E} = \mathbf{E}_0 e^{i(\mathbf{k}\cdot\mathbf{r} - \omega t + \phi)} \tag{1}$$

The radiation consists of wave trains with different lifetimes, and the average lifetime τ_0 is called the coherence time, see figure 2. The wave trains differ in phase because of the random processes producing the light, e.g. thermal excitation. Depending on the source, the produced light will have frequencies ω within a certain frequency spectrum. Using Fourier analysis, one has that [2]

$$\Delta\omega = \frac{2\pi}{\tau_0} \tag{2}$$

where $\Delta\omega$ is a measure of the spectral line width. From this it is seen that a broadband source with a large $\Delta\omega$ has a short coherence time τ_0.

The coherence length l_t of a wave train is $l_t = c\tau_0$, [2], where c is the speed of the wave. Using equation (2) we get $l_t = c2\pi/\Delta\omega = c/\Delta\nu$. Using the relation $\nu_0 = c/\lambda_0$ where ν is the optical frequency, and approximating $\Delta\nu$ by the magnitude of its differential,

$$\frac{\Delta\nu}{\Delta\lambda} \approx \left|\frac{d\nu}{d\lambda}\right| = \frac{c}{\lambda^2} \tag{3}$$

we get $l_t \approx \frac{\lambda_0^2}{\Delta\lambda}$ where $\Delta\lambda$ is a measure of the line width and λ_0 is the center wavelength. This is only a somewhat intuitive derivation of the coherence length, and a precise definition is given in the next section.

2.2 Interference

We now consider the propagation of two beams $\mathbf{E}_1(\mathbf{r},t)$ and $\mathbf{E}_2(\mathbf{r},t)$ from the same source, travelling different paths. If the beams meet at a point P and one beam has travelled the extra time τ, the resultant field at P is

$$\mathbf{E}_P(t) = \mathbf{E}_1(t) + \mathbf{E}_2(t+\tau) \tag{4}$$

using the principle of superposition. Inserting equation (1) and setting $\mathbf{r}$ and ϕ to 0 for convenience: $\mathbf{E}_P(t) = \mathbf{E}_{01}e^{-i\omega t} + \mathbf{E}_{02}e^{-i\omega(t+\tau)}$. The power per unit area at P is given by the Poynting vector $\mathbf{S} = \varepsilon_0 c^2 \mathbf{E}_P \times \mathbf{B}_P$ [2]. Since $\mathbf{E}_P$ and $\mathbf{B}_P$ are rapidly varying fields ($\sim 10^{14}$ Hz for 1550nm light), the power per unit area (irradiance) I_P measured by a detector at P would be a time average of $\mathbf{S}$: $I_P = \langle|\mathbf{S}|\rangle = \varepsilon_0 c^2 \langle|\mathbf{E}_P \times \mathbf{B}_P|\rangle$. From electromagnetic theory we know that $\mathbf{E}$ and $\mathbf{B}$ are orthogonal and that $|\mathbf{E}| = c\,|\mathbf{B}|$ [2]. This gives $I_P = \varepsilon_0 c \left\langle |\mathbf{E}_P|^2 \right\rangle = \varepsilon_0 c \langle \mathbf{E}_P \cdot \mathbf{E}_P^* \rangle$. Inserting equation (4) we get

$$\begin{aligned} I_P &= \varepsilon_0 c \langle (\mathbf{E}_1 + \mathbf{E}_2) \cdot (\mathbf{E}_1^* + \mathbf{E}_2^*) \rangle \\ &= \varepsilon_0 c \left\langle |\mathbf{E}_1|^2 + |\mathbf{E}_2|^2 + (\mathbf{E}_1 \cdot \mathbf{E}_2^* + \mathbf{E}_2 \cdot \mathbf{E}_1^*) \right\rangle \end{aligned}$$

Omitting the constant multiplicative factor $\varepsilon_0 c$ and writing the irradiances of the individual beams as I_1 and I_2: $I_P = I_1 + I_2 + 2\,\mathrm{Re}\,\langle \mathbf{E}_1(t) \cdot \mathbf{E}_2^*(t+\tau) \rangle$ using A + A* = 2Re(A). From this it is seen that *if the two beams have the same polarization*, the dot product maximizes: $\langle \mathbf{E}_1(t) \cdot \mathbf{E}_2^*(t+\tau) \rangle = \langle E_1(t) E_2^*(t+\tau) \rangle$. Defining a correlation function $\mathbf{\Gamma}_{12}(\tau) \equiv \langle E_1(t) E_2^*(t+\tau) \rangle$ and a normalized correlation function $\boldsymbol{\gamma}_{12}(\tau) \equiv \frac{\mathbf{\Gamma}_{12}(\tau)}{\sqrt{I_1 I_2}}$ [2] we get

$$I_P = I_1 + I_2 + 2\sqrt{I_1 I_2}\,\mathrm{Re}\,[\boldsymbol{\gamma}_{12}(\tau)] \tag{5}$$

A known result from statistical optics is that $\boldsymbol{\gamma}_{12}(\tau)$ can be expressed as [3]

$$\boldsymbol{\gamma}_{12}(\tau) = \int_0^\infty S(\nu) e^{-i2\pi\nu\tau} d\nu$$

where $S(\nu)$ is a normalized[1] power spectral density of the light source. The complex degree of coherence $\boldsymbol{\gamma}_{12}(\tau)$ can thus be viewed as a Fourier transform of the power spectrum, as defined in [4]. When the power spectral density is an even function of $(\nu - \nu_0)$, the complex coherence can be written as a product of a real-valued factor and $e^{-i2\pi\nu_0\tau}$ [3]: $\boldsymbol{\gamma}_{12}(\tau) = \gamma_{12}(\tau) e^{-i2\pi\nu_0\tau}$. This gives

$$I_P = I_1 + I_2 + 2\sqrt{I_1 I_2}\gamma_{12}(\tau)\cos(2\pi\nu_0\tau) \tag{6}$$

[1] normalized in the sense that $\int_0^\infty S(\nu)d\nu = 1$, [3]

From this we see that the intensity will vary sinusoidally with τ, modulated with an envelope function γ_{12} determined by the Fourier transform of the spectrum. Assuming that τ_0 is a constant coherence time and not an average, one can show that for harmonic waves with frequency ω_0 [2]: $\mathrm{Re}\left[\boldsymbol{\gamma}_{12}(\tau)\right] = \left(1 - \frac{\tau}{\tau_0}\right)\cos(\omega_0\tau)$ (for $\tau \leq \tau_0$) giving

$$\begin{aligned} I_P &= I_1 + I_2 + 2\sqrt{I_1 I_2}\left(1 - \frac{\tau}{\tau_0}\right)\cos(\omega_0\tau) \\ &= I_1 + I_2 + 2\sqrt{I_1 I_2}\left(1 - \frac{\Delta l}{l_t}\right)\cos(k_0\Delta l) \end{aligned} \tag{7}$$

using $\tau = \Delta l/c$ where Δl is the difference in optical path length for the two beams, and $k_0 = 2\pi/\lambda_0$ where λ_0 is the wavelength of the waves. For $\tau > \tau_0$ the interference term vanishes because the random phase variations cancel out: $I_P = I_1 + I_2$. From this it is seen that the optical path difference Δl must be smaller than the coherence length l_t in order to observe interference fringes.

The factor $\gamma_{12}(\tau) = \left(1 - \frac{\Delta l}{l_t}\right)$ comes from the assumption of constant coherence time τ_0. If instead the spectrum of the source is Gaussian, one obtains for the coherence function [3]

$$\gamma_{12}(\tau) = \exp\left[-\left(\frac{\pi\Delta\nu\tau}{2\sqrt{\ln(2)}}\right)^2\right] \tag{8}$$

which as expected is Gaussian, since the Fourier transform of a Gaussian function is itself a Gaussian function. $\Delta\nu$ is the FWHM of the normalized spectrum. It is seen that the maximum of $\gamma_{12}(\tau)$ is 1 and occurs when $\tau = 0$. Defining the coherence length $l_t = \tau_0 c$ with the condition $\gamma_{12}(\tau_0) = \frac{1}{2}$ gives

$$l_t = \frac{2\ln(2)}{\pi}\frac{c}{\Delta\nu} = \frac{2\ln(2)}{\pi}\frac{\lambda^2}{\Delta\lambda} \approx 0.44\frac{\lambda^2}{\Delta\lambda} \tag{9}$$

which is sometimes used in the OCT litterature [5]. $\Delta\lambda$ is the FWHM of the spectrum measured in wavelength units.

If the coherence time is instead defined as the power-equivalent width (as defined in [6]) of the coherence function, the result is [3]

$$l_t = \sqrt{\frac{2\ln(2)}{\pi}}\frac{\lambda^2}{\Delta\lambda} \approx 0.66\frac{\lambda^2}{\Delta\lambda} \tag{10}$$

This definition is most widely used in the OCT litterature [7].

Since the coherence length is a measure of the width of the signal envelope, it is a reasonable estimate for the depth (axial) resolution in OCT: if the distance between two reflecting planes in the medium is smaller than the coherence length, the interference signals arising from each of the two planes will overlap, resulting in a smearing of the image contrast.

3 SNR analysis in OCT systems

3.1 Statistical properties of noise

When performing OCT, the measured signal unavoidably contains noise. Determining the signal as a current gives $I_s^{meas} = I_s^{true} + I_{noise}$, where I_s^{meas} is the measured signal and I_s^{true} is the "true" signal. Since any constant property of the noise does not affect the qualitative property of an OCT image, and assuming

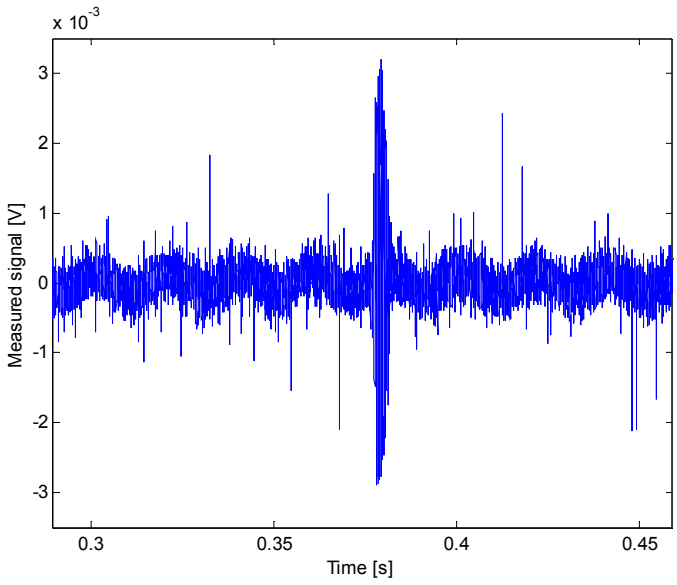

Figure 3. A measured (weak) signal at $0.38s$ *and the surrounding noise. The signal maximum* $V_{s,\max} = 3.2mV$*, and the noise rms value* $\sigma_v = 0.21mV$*. The 50Hz noise is easily seen.*

the noise to be of random nature, the time average of the noise must be zero: $\langle I_{noise} \rangle = 0$. An often used measure of the noise [8] is the root-mean-square (rms) standard deviation σ or the mean-square variance σ^2, in the case of a current signal: $\sigma_i^2 = \langle I_{noise}^2 \rangle$. This is calculated as [9]:

$$\sigma_i^2 = \frac{1}{N} \sum_{n=1}^{N} \left(I_{noise,n} \right)^2$$

where N is the number of measurements, and $I_{noise,n}$ is the n'th measurement.

Depending on the application of the OCT-system, one can imagine different views of "signal" and "noise". For instance, if one is only interested in measuring the thickness t of a homogenous medium very precisely, the size of the noise floor σ_i of the measured signal is not really important as long as it is smaller than the signal I_s from the reflection at the medium boundaries. Instead, one could make N measurements and determine a measure for the noise as $\sigma_t^2 = \frac{1}{N} \sum_{n=1}^{N} \left(t_n - t \right)^2$ where t is the measured average ("true") thickness of the sample. In this perspective, an important source of noise would be the imperfect mechanical scanner reference arm. Likewise, one would consider the distance t between the reflections from the front and back of the sample to be the "signal".

We will primarily focus on the application of OCT for imaging, and will therefore adopt a different view. To obtain a good image of an object in a medium, where it is possible to distinguish different features, one needs a high *contrast*. When the optical path difference (OPD) between the mirror and the object of interest is zero, the detection system generates a signal current $I_{s,\max}$. As the OPD increases beyond the coherence length, the detection system no longer measures the true signal, but the noise σ_i^2 inherent in the system, see figure 3 (the spectrum of this signal can be seen in figure 17).

One would achieve good contrast if the signal current I_s is much larger than the background noise σ_i^2. A popular definition of the signal-to-noise ratio, SNR,

is therefore [5], [10]

$$SNR = \frac{I_s^2}{\sigma_i^2} \tag{11}$$

where we choose to define the SNR as

$$SNR = \frac{I_{s,\max}^2}{\sigma_i^2} \tag{12}$$

because only the maximum of the interference signal indicates the location of the change in refractive index in the medium. When measured in dB, we use $SNR = 10\log_{10}\left(\frac{I_{s,\max}^2}{\sigma_i^2}\right)$.

3.2 Noise considerations

The signal photocurrent in equation (11) is the coherent part of the signal backscattered from the sample given by $I_s = 2\rho\sqrt{P_r P_s}\gamma_{12}(\tau)\cos(2\pi\nu_0\tau)$, where ρ is the detector responsivity, P_r is the power impinging on the photodetector reflected from the mirror and P_s is the coherent portion of the power incident on the photodetector having been backscattered from the sample. Since this function has a maximum at $\tau = 0$, the maximum-squared signal photocurrent in a single detector becomes

$$I_{s,\max}^2 = 4\rho^2 P_r P_s \tag{13}$$

For a balanced reciever the total photocurrent is the sum of the photocurrent in each detecter, so the maximum-squared signal photocurrent is [10]

$$I_{s,\max}^2 = 16\rho^2 P_r P_s \tag{14}$$

The noise sources of greatest interest are the reciever noise, the shot noise and the intensity noise/beat noise [10].

Receiver noise

The reciever noise is the noise in the detector. It consists of shot noise, thermal noise, amplifier noise and temperature noise [11].

The *shot noise* arises from the background light and the dark current in the detector. This contribution to the detector noise can be neglected, since it is generally small [10].

The *thermal noise* stems from the random thermal motion of electrons in a conductor and is given by

$$\sigma_{th}^2 = 4k_B TB/R_{\text{eff}}$$

where k_B is Boltzmann's constant, T is the temperature and B is the detection bandwidth. R_{eff}, the effective load resistance, can in this case not be found because of the complexity of the electronic circuits in the detector.

The *temperature noise* is caused by the random fluctuations in temperature due to the statistical nature of the heat transfer between the detector and its environment. The temperature noise given as the mean square radiant power fluctuations is [11]

$$\Delta\Phi_{temp}^2 = 4k_B T^2 KB$$

If it is assumed that the background is in equilibrium with the detector, $K = 4\epsilon\sigma T^3 A$, where ϵ is the permeability, σ is Stefan-Boltzmans constant and A is the detector area.

The *amplifier noise* is given by

$$\sigma_{amp}^2 = G^2 4k_B(T_A + T_D)B/R_{\text{eff}}$$

where G is the gain of the amplifier, T_A is the amplifier noise temperature and T_D is the noise temperature of the detector load resistance.

Several of the parameters in the reciever noise term are difficult to evaluate and another expression for the reciever noise is preferred. This can be found by using the input current noise (INC) or the noise equivalent power (NEP) obtained from the manufacturer specifications [12], $INC = 3pA/\sqrt{Hz}$, from which an estimate for the reciever noise is calculated as [10]

$$\sigma_{re}^2 = \left(3pA/\sqrt{Hz}\right)^2 B$$

Notice, that since this is only the noise from the photodiode, this value will be considerably lower than the actual reciever noise.

Photon shot noise

Photon shot noise arising from the signal is caused by quantisation of the light, i.e. the photocurrent consists of photons with a certain energy, and therefore it does not "float" as a continuos medium. Thus, the random arrival of photons is detected as noise. The photon shot noise can be written as [10]

$$\sigma_{sh}^2 = 2qI_{dc}B$$

where q is the free electron charge, and I_{dc} is the mean detector photocurrent given by

$$I_{dc} = \rho(P_r + P_x) \tag{15}$$

assuming that $P_r, P_x >> P_s$. Here, P_x is the power of the incoherent light backscattered from the sample and arriving at the detector. Therefore, the shot noise is always present with a photocurrent.

Excess intensity noise and beat noise

An excess intensity noise arises from the time fluctuations of the intensity and is given by [10]

$$\sigma_{ex}^2 = (1 + V^2)I_{dc}^2 B/\triangle\nu$$

where V is the degree of polarization of the source and $\triangle\nu$ is the effective linewidth of the source, given by $\Delta\nu = \sqrt{\frac{\pi}{2\ln(2)}}c\frac{\Delta\lambda}{\lambda_0^2}$ where $\Delta\lambda$ is the FWHM wavelength bandwidth of the spectrum.

The total photocurrent variance can now be obtained by summing all independent contributions [9]

$$\sigma_i^2 = \sigma_{re}^2 + \sigma_{sh}^2 + \sigma_{ex}^2$$

Using the expressions for shot noise and excess intensity noise and setting $\sigma_{sh}^2 = \sigma_{ex}^2$, it is found that the excess intensity noise will dominate over the shot noise when $I_{dc} \gtrsim 4\mu A$. If balanced detection is used, the excess intensity noise is suppressed. This is shown in the following calculations.

The electric fields after they have been mixed in a 50-50 beam splitter are assuming r = $\phi = 0$ for simplicity, (see figure 4) [13]

$$\mathbf{E}_+ = \frac{1}{\sqrt{2}}(\mathbf{E}_{01}e^{-i\omega t} + \mathbf{E}_{02}e^{-i\omega t - \frac{\pi}{2}i})$$

$$\mathbf{E}_- = \frac{1}{\sqrt{2}}(\mathbf{E}_{01}e^{-i\omega t - \frac{\pi}{2}i} + \mathbf{E}_{02}e^{-i\omega t})$$

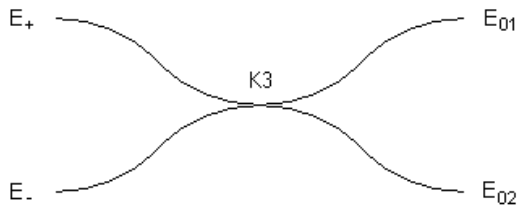

Figure 4. Closeup of the double detection. $\boldsymbol{E}_{01}$ *and* $\boldsymbol{E}_{02}$ *are the input electric fields from the sample and reference respectively, and* $\boldsymbol{E}_{+}$ *and* $\boldsymbol{E}_{-}$ *are the output electric fields.* $K_3 = \frac{1}{2}$

Hence, the irradiance is given by (ignoring the prefactor $\epsilon_0 c^2$)

$$\begin{aligned} I_+ &= \left\langle |\mathbf{E}_+|^2 \right\rangle = \frac{1}{2}\left\langle (|\mathbf{E}_{01}|^2 + |\mathbf{E}_{02}|^2 + \mathbf{E}_{01}\mathbf{E}_{02}^* e^{-i\omega t} e^{i\omega t} e^{\frac{\pi}{2}i} + \mathbf{E}_{01}^* \mathbf{E}_{02} e^{i\omega t} e^{-i\omega t} e^{-\frac{\pi}{2}i}) \right\rangle \\ &= \frac{1}{2}\left\langle (|\mathbf{E}_{01}|^2 + |\mathbf{E}_{02}|^2 + \mathbf{E}_{01}\mathbf{E}_{02}^* e^{\frac{\pi}{2}i} + \mathbf{E}_{01}^* \mathbf{E}_{02} e^{-\frac{\pi}{2}i}) \right\rangle \\ I_- &= \left\langle |\mathbf{E}_-|^2 \right\rangle = \frac{1}{2}\left\langle (|\mathbf{E}_{01}|^2 + |\mathbf{E}_{02}|^2 + \mathbf{E}_{01}\mathbf{E}_{02}^* e^{i\omega t} e^{-i\omega t} e^{-\frac{\pi}{2}i} + \mathbf{E}_{01}^* \mathbf{E}_{02} e^{-i\omega t} e^{i\omega t} e^{\frac{\pi}{2}i}) \right\rangle \\ &= \frac{1}{2}\left\langle (|\mathbf{E}_{01}|^2 + |\mathbf{E}_{02}|^2 + \mathbf{E}_{01}\mathbf{E}_{02}^* e^{-\frac{\pi}{2}i} + \mathbf{E}_{01}^* \mathbf{E}_{02} e^{\frac{\pi}{2}i}) \right\rangle \end{aligned}$$

When the signals are subtracted in the balanced detector, the two intensity terms are cancelled while the interference terms remain

$$\begin{aligned} I_+ - I_- &= \frac{1}{2}\left\langle \mathbf{E}_{01}\mathbf{E}_{02}^*(e^{\frac{\pi}{2}i} - e^{-\frac{\pi}{2}i}) - \mathbf{E}_{01}^*\mathbf{E}_{02}(e^{\frac{\pi}{2}i} - e^{-\frac{\pi}{2}i}) \right\rangle \\ &= i\left\langle (\mathbf{E}_{01}\mathbf{E}_{02}^* - \mathbf{E}_{01}^*\mathbf{E}_{02}) \right\rangle \end{aligned}$$

The cancellation of the intensity terms explains why the intensity noise is suppressed. The remaining term, the interference term, however gives rise to another noise source. This is named *beat noise* and is given as [10]

$$\sigma_{be}^2 = 8\rho^2(1+V^2)P_r P_x B/\triangle\nu$$

where P_r and P_x are the powers impinging on one of the two detectors in balanced detection.

Hence, in a balanced system the total photocurrent variance or noise is therefore replaced by

$$\sigma_i^2 = \sigma_{re}^2 + \sigma_{sh}^2 + \sigma_{be}^2$$

Unbalanced system

The unbalanced system contains a Michelson interferometer as shown in figure 5. For an unbalanced system the coherent part of the power backscattered from the sample and impinging on the detector, P_s is given by [10], [14]

$$P_s = P_{so}K(1-K)\Gamma_s$$

where K is the splitting ratio and P_{so} is the power of the light from the source. Γ_s is the reflection coefficient of the sample, corresponding to that fraction of backscattered light, coherent with the reference light.

The incoherent part of the power backscattered from the sample and arriving at the detector, P_x is given by

$$P_x = P_{so}K(1-K)\Gamma_x$$

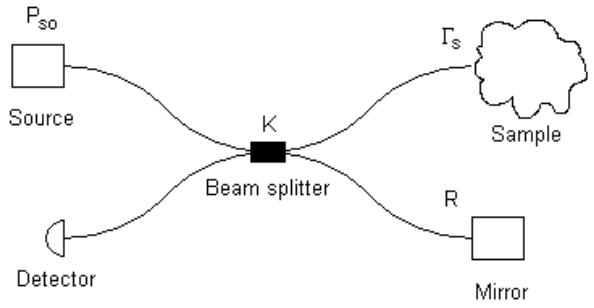

Figure 5. The unbalanced OCT system

where Γ_x is the reflection coefficient of the sample, corresponding to that fraction of backscattered light, incoherent with the reference light. The power from the reference arm, measured at the detector, P_r is given by

$$P_r = P_{so}(1-K)KR$$

where R is the mirror reflectivity. Using equation (15) the shot noise and the excess intensity noise is given by

$$\begin{aligned} \sigma_{sh}^2 &= 2qI_{dc}B = 2q\rho(P_r + P_x)B \\ \sigma_{ex}^2 &= (1+V^2)I_{dc}^2 B/\triangle\nu \end{aligned}$$

The receiver noise is for unbalanced as well as balanced systems

$$\sigma_{re}^2 = \left(3pA/\sqrt{Hz}\right)^2 B$$

The optimal splitting ratio of the coupler in the unbalanced system (fig. 5) can easily be calculated. If the ratio is K, then the amount of power P_s to reach the detector from the sample must be $P_s \propto K(1-K)$. To maximize this power the derivative is found and put equal zero.

$$\frac{d}{dK}K(1-K) = 1 - 2K = 0$$

which of course gives $K = \frac{1}{2}$. The same calculation can be made for the power from the reference, giving the same result, so both the power from the sample and the reference is maximized for $K = \frac{1}{2}$. This is also intuatively obvious since the light to both the sample and reference must pass the coupler once in each direction.

Balanced system

A balanced system is an extended version of the unbalanced system. Two more beamsplitters are incorporated in order to introduce double detection.

Looking at a balanced system as shown in figure 6, where the attenuator in front of one of the detectors is excluded from the following model, the powers impinging on each detector now becomes

$$\begin{aligned} P_s &= \frac{1}{2}P_{so}K_1(1-K_1)\Gamma_s \\ P_x &= \frac{1}{2}P_{so}K_1(1-K_1)\Gamma_x \\ P_r &= \frac{1}{2}P_{so}(1-K_1)K_2(1-K_2)R \end{aligned}$$

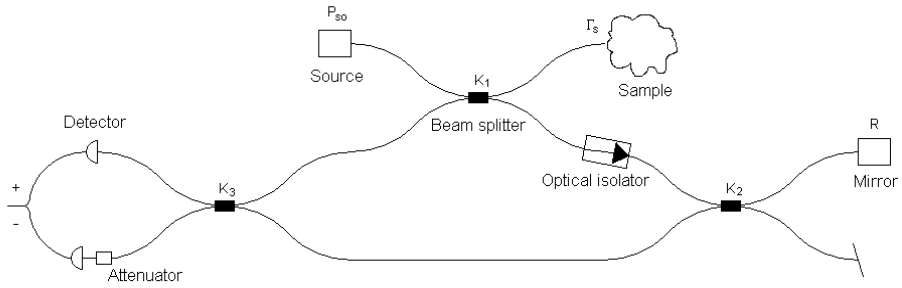

Figure 6. The balanced OCT system with attenuator

The isolator between K_1 and K_2 is necessary to ensure that power coupled back from the reference mirror is not coupled back through K_1 to the detector thus increasing shot noise and beat noise. The prefactor $\frac{1}{2}$, is the splitting ratio K_3, which has to have this value in order to assure that the intensity noise is suppressed. The shot noise and the beat noise is

$$\begin{aligned} \sigma_{sh}^2 &= 4qI_{dc}B = 4q\rho(P_r + P_x)B \\ \sigma_{be}^2 &= 8(1+V^2)\rho^2 P_r P_x B/\triangle\nu \end{aligned}$$

A 3 dB attenuator could be added in one detector arm, since it would improve the detection efficiency (the common-mode rejection is maximized when the power in the reference input of the detector is two times that in the signal input [12]).

When the attenuator is added to the system, the photocurrent is replaced by $I_s = (1+d)2\rho\sqrt{P_r P_s}\gamma_{_{12}}(\tau)\cos(2\pi\nu_0\tau)$, where d is the attenuation factor, which is $\frac{1}{2}$ for a 3dB attenuator. Thus, the maximum-squared photocurrent becomes

$$I_{s,\max}^2 = 4(1+d)^2\rho^2 P_r P_s$$

and shot noise and beat noise changes to

$$\begin{aligned} \sigma_{sh}^2 &= (1+d)2q\rho(P_r + P_x)B \\ \sigma_{be}^2 &= (1+d)^2 \cdot 2(1+V^2)\rho^2 P_r P_x B/\triangle\nu \end{aligned}$$

Another type of a balanced system is shown in figure 7. The addition of a fourth beamsplitter entails an additional loss of power. However, the advantage of the system is that the length of the reference and sample arms are equal. The powers are ($K_4 = \frac{1}{2}$)

$$\begin{aligned} P_s &= \frac{1}{2}P_{so}K_1K_2(1-K_2)\Gamma_s \\ P_x &= \frac{1}{2}P_{so}K_1K_2(1-K_2)\Gamma_x \\ P_r &= \frac{1}{2}P_{so}(1-K_1)K_3(1-K_3)R \end{aligned}$$

A model based on the above calculations is presented in section 5.2.

4 CW sources for OCT systems

In an OCT system the spectrum of the source is very important as it determines the maximum resolution of the image. The dependence of the spectrum is ex-

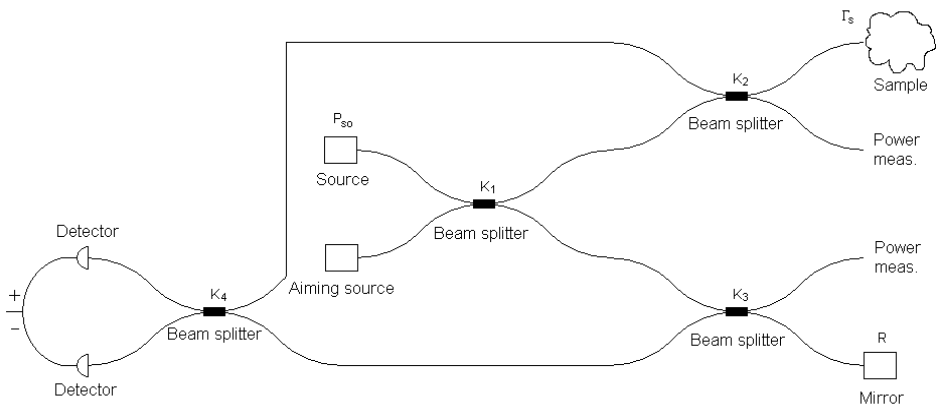

Figure 7. Sketch of a balanced system with four beam splitters

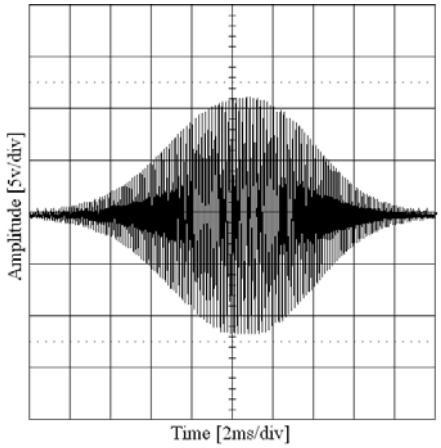

Figure 8. An example of a signal from the OCT system as seen on an oscilloscope. The source used is the Giga 1540nm SLD. The scanner speed is 6mm/s.

plained in section 2.2. An example of a signal from an OCT system is seen in figure 8. To characterize a given spectrum the source must be described, which is done below.

4.1 Overview of sources

Different sources has been used in OCT, but common to all is that they uses one of two ideas: time-of-flight (TOF) measurements or frequency domain measurements. The sources used for TOF emphasizes the temporal characteristics of the source, which means that these sources must be pulsed. One advantage of these sources is that the spectral characteristics of the source is not that important, although dispersion and wavelengths must still be kept in mind. Sources used for these measurements are gated lasers [1].

Frequency domain measurements emphasizes the spectral characteristics of a given source. Here coherence length, wavelength and power are important issues. Sources used for frequency measurements must have wide linewidths to give them a short coherence length, as seen in equation (10). The wavelength of the sources must be chosen for the application, but since higher wavelengths tend to penetrate

deeper in tissue (because of less scattering [7]), these are generally preferred. The power of the sources can pose a limit, if superluminescent diodes [15] are used, since these are typically in the mW range. Another type of sources that can be used for frequency domain measurements is scanning sources. By using these source the scanning action of the system is moved from the reference to the source, by rapidly tuning the frequency of the source [16].

4.2 Superluminescent diodes

The OCT system depends on the broad light-spectrum of the source which makes the μm-resolution possible. In this system a superluminescent diode (SLD) is used and one of these is a SLD from the company Giga. This SLD is a MQW or multiple-quantum-well diode. The diode is edge-emitting and the facets are angled at 7° with the cavity dimensions being: length 980 μm, width 500 μm and height 100 μm. We have also used a SLD from the Russian company Superlum, due to the breakdown of the Giga diode in a power failure. Since the Superlum diode is a commercial product the exact design details for the SLD is kept secret by the company, but the spectral linewidth is given as 59nm with a center wavelength of 1545nm. The last SLD used is a 1300nm diode from the company AFC.

What gives the SLD the broad spectrum is the angled facets of the diode (in the case of the Giga SLD) which keeps it from beginning to lase. The light in the diode is reflected at an angle so that only a small amount of it actually stays in the diode thus keeping any one mode from becoming dominant. This design means that the light from the diode is still amplified in the diode-cavity, but no mode-selection happens during this amplification, however modes are still present.

The modes are closely spaced and since the feedback is so small the individual modes will normally not be seen. The mode-spacing is determined by the SLD geometry and can be found through simple calculations.

The wave-length λ and frequency ν of light is related as [2]

$$\nu = \frac{c}{\lambda} = \frac{c_0}{n\lambda} \tag{16}$$

The speed of light is written as $c = \frac{c_0}{n}$, with n being the refractive index. By using equation (3) the frequency difference between two modes can be approximated:

$$\Delta\nu = \frac{c_0}{n}\frac{\Delta\lambda}{\lambda^2} \tag{17}$$

Because of the feedback in the cavity itself, only an integer amount of half wavelengths are contained within the diode. The number of these standing waves in the cavity can be written as

$$\frac{\lambda}{2}N = Ln$$

where N is an integer, L is the cavity length and n is the refractive index of the active SLD material. Rewriting this we get $\lambda = \frac{2Ln}{N} = \frac{c_0}{n\nu}$ or in terms of ν

$$\nu = \frac{c_0 N}{2Ln^2}$$

The spacing between two modes must then be

$$\Delta\nu = \frac{c_0}{2Ln^2}(N - (N-1)) = \frac{c_0}{2Ln^2} \tag{18}$$

By setting eqn. (17) and eqn. (18) equal to each other, an expression for the mode spacing can be found

$$\frac{c_0}{2Ln^2} = \frac{c_0}{n}\frac{\Delta\lambda}{\lambda^2}$$

rewriting this gives

$$\Delta\lambda = \frac{\lambda^2}{2Ln} \tag{19}$$

This mode-spacing was found experimentally in the Giga SLD as shown in the next section.

4.3 Measurements of the spectra

The spectrum of the input beam is important for many reasons, one of which is the axial resolution. The axial resolution dependence arises from the Fourier duality: the wider the input spectrum, the narrower the transformed spectrum is, i.e. a large spectral linewidth gives a short coherence length, as seen in equation (10). The measurement of the spectrum can be found in the sections below.

As mentioned earlier, the envelope of the detected signal in an OCT system is the Fourier transform of the input beams optical spectrum. This means that the shape of the SLD spectrum is important because a "strange" spectrum can be hard to decipher in the output signal.

The easiest spectrum to handle is the Gaussian since the Fourier transform of a Gaussian is another Gaussian. The problem arises when a spectrum is not perfectly Gaussian because of the so called side lobes, so that if the OCT output consists of several signals close to each other the side lobes of one signal can be hard to distinguish from a smaller separate signal. This is also the reason why companies producing SLD's go to great lengths to reduce the size of side-lobes.

Giga SLD

The measurement of the SLD spectrum is done using an Optical Spectrum Analyzer (OSA). Three different settings of the temperature controller for the SLD were used in the measurements. The temperature resistances were 12, 15 and 18$k\Omega$ which corresponds to 20, 15 and 10°C respectively. Furthermore a series of measurements were taken with varying spans - the span determines the wavelength resolution of the measurement.

The first measurement was at 12$k\Omega$ and with a span of 200nm, which is shown in figure 9. The left plot is the spectrum measured with the OSA and is recorded in dBm/nm, where dBm is defined as $10 \cdot log_{10}(\frac{P}{1mW})$ where P is the measured power. Since the spectrum is expected to be close to a Gaussian, the spectrum can be converted to a linear representation as seen in the right plot of fig. 9. Here the spectrum has been fitted to a Gaussian with reasonable succes, although there are a lot of oscillations deviating from the fitted Gaussian, especially around the top. These oscillations are evidence of the simple construction of the SLD lacking suppression of the individual modes of the cavity.

Some of the characteristics of the spectrum in fig. 9 is the center wavelength and the spectral linewidth. The center wavelength is 1540nm and the spectral linewidth, defined as the FWHM, is 20nm. Using equation (10) this gives a coherence length of 78μm, and using equation (9) a coherence length of 52μm is calculated. The FWHM of the envelope in figure 8 should correspond to the coherence length when defined as in equation (9), and is estimated to 48μm which shows excellent agreement with the calculated 52μm.

As mentioned in section 2.2 an interference signal consisting of a cosine modulated by the Fourier-transform of the spectrum is measured. Knowing this makes it interesting to see what the FFT of the spectrum looks like. In figure 10 the Gaussian seems to fit the FFT quite well. The plot also shows some side lobes located symmetrically around the center peak. As before a Gaussian is fitted to

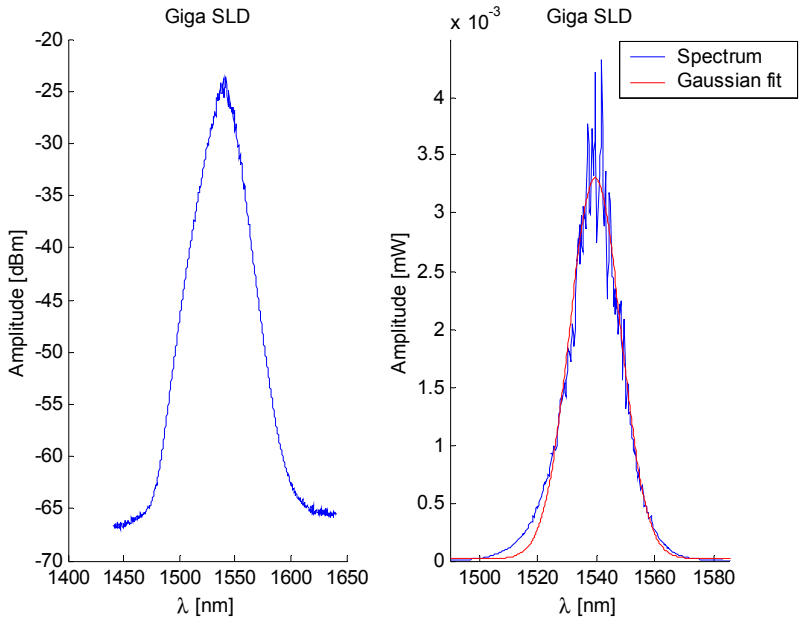

Figure 9. Left: Logarithmic plot of the Giga SLD spectrum. Right: Linear plot of the spectrum with a Gaussian fit.

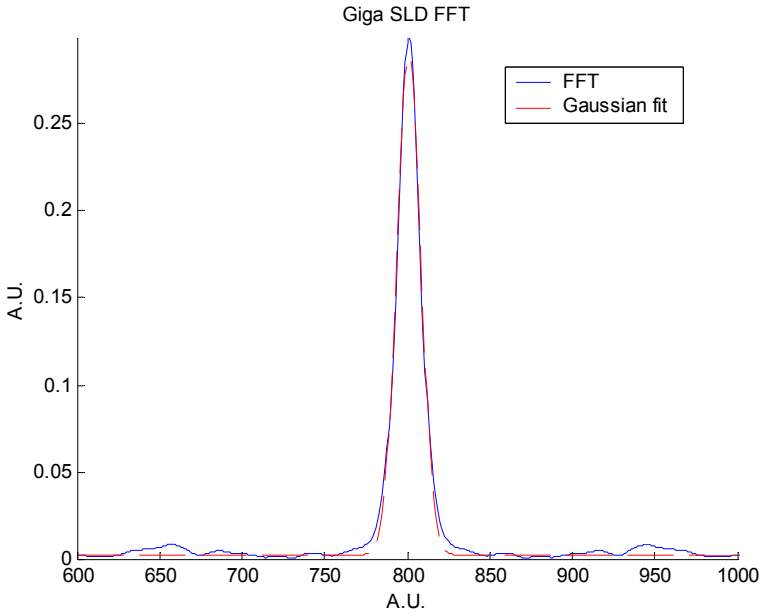

Figure 10. This plot shows the FFT of the spectrum from the Giga SLD at a temperature of 20°C, and a Gaussian fit.

the FFT of the spectrum. This time there is a very good match between the two plots which means that the ripples observed in the spectrum of the SLD do not seem to be a problem, although the side lobes might pose a problem.

As mentioned the measurement was repeated at different temperatures. These measurements were almost indistinguishable from the one in fig. 9, which means that the SLD spectrum is relativly stable over these temperatures.

Some differences were observed though. The center wavelength drops by $5nm$ to around $1535nm$ when the temperature is decreased to $10°C$, and the spectral

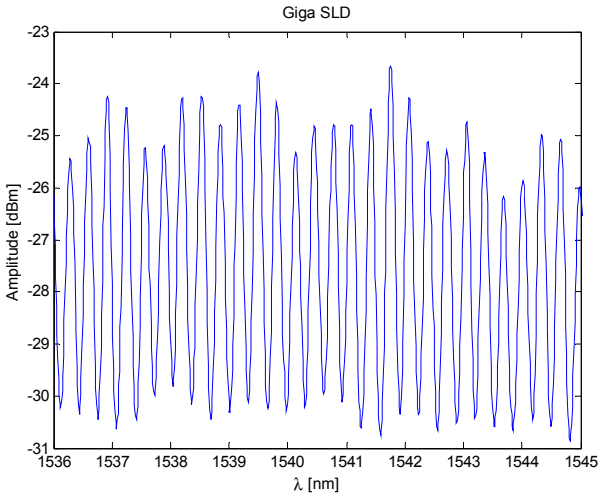

Figure 11. This plot show a closeup of the center of the Giga SLD spectrum. The temperature was 20°C and the span was 10 nm.

linewidth decreases by about $1nm$ for each $5°C$ the temperature is lowered. These differences are countered by the increase in the output power of the SLD at lower temperatures.

Another measurement was carried out at a span of just $10nm$ and here an interesting phenomenon was seen (figure 11).

The ripples in the plot are caused by the mode-spacing of the SLD, and are approximately 0.3 nm apart. Comparing with the theory (eqn. 19) we get

$$\Delta\lambda = \frac{\lambda^2}{2Ln} = \frac{(1540nm)^2}{2 \cdot 980\mu m \cdot 3.54} = 0.34nm$$

where the correspondence between the theory and measurement is very good.

At all these measurements the background noise was also recorded with the source switched off, but the noise floor is so low that it makes no difference if it is subtracted from the real measurements. So in all the plots the background noise has been neglected.

Superlum SLD

Again the spectrum was measured with an OSA. Unlike the Giga SLD where both the temperature and the current could be varied, only the current can be altered with the Superlum SLD due to operational specifications.

The measurements on the Superlum diode were taken at three different current settings - 290, 200 and $100mA$. The first one at $290mA$ is the "most important" one in the sense that the SLD will be driven at this maximum current when operating. The spectrum at this current was recorded with at span of $300nm$ giving the plot in figure 12. The spectrum is very close to a true Gaussian shape with a center wavelength of $1547nm$ and a FWHM of approximately $62nm$, which is very close to the manufacturer specifications of $1545nm$ center wavelength and a FWHM of $59nm$. The Fourier-transform of the spectrum is also very close to a Gaussian (as it should be), and the detected signal should be very well behaved with this diode, since there are no side lobes in the FFT to disturb the detected signal - at least they are not visible on the scales used. The coherence length calculated with equation (9) is $17\mu m$. The FWHM of the envelope in figure 13 should correspond to this, and is estimated to $19.2\mu m$ which again shows excellent agreement.

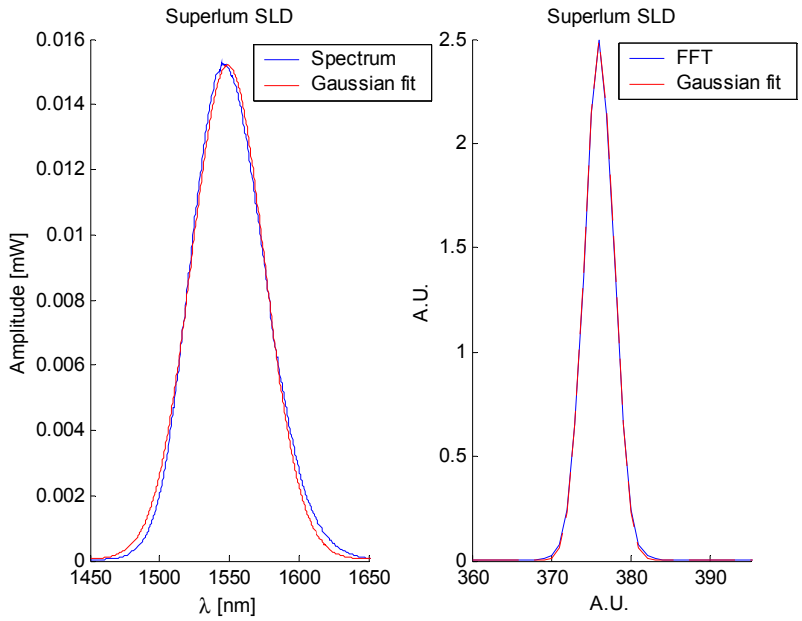

Figure 12. The spectrum of the Superlum SLD at 290mA and a span of 300nm. The left plot is a linear version of the spectrum, where the right one is the FFT-transform. Both plots have a Gaussian fitted to it.

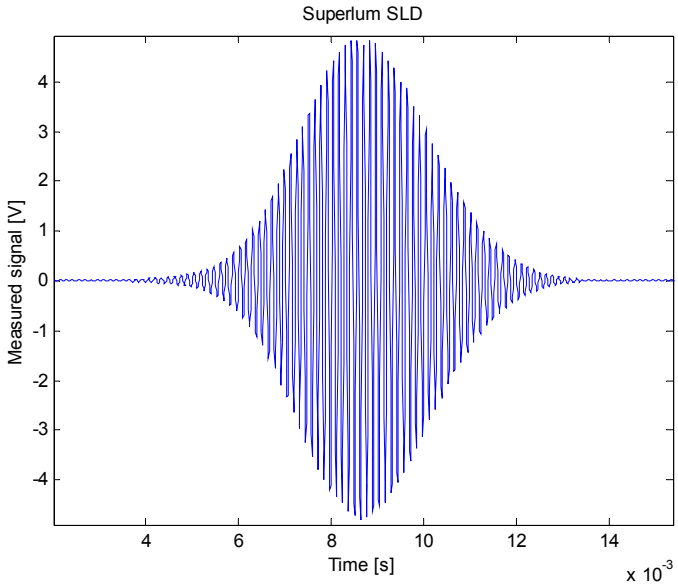

Figure 13. A measured signal with the Superlum SLD when mirrors were used in both reference and sample arm. The scanner speed is 6mm/s.

Repeating the above measurement at $100mA$ gives the spectrum in fig. 14. Closer inspection of figures 12 and 14 shows that the center wavelength of the spectrum is dependent on the current through the diode. At $100mA$ the center is at $1572nm$ which is a difference of $25nm$ as compared to the $290mA$ spectrum. The width of the spectrum on the other hand changes very little, but seems to increase slightly (around $2nm$) when the current is increased from $100mA$ to $290mA$.

Again the background noise was recorded with the SLD switched off, and as

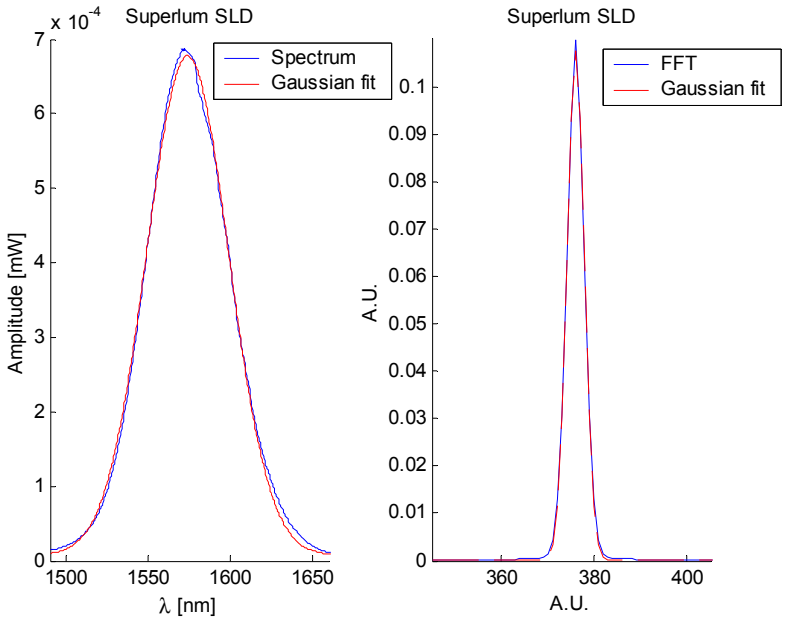

Figure 14. Left: The spectrum at 100mA current applied to the SLD. Right: FFT of the spectrum. Both plots have a Gaussian fitted.

before the noise found was around 4-6 decades weaker than the signal itself.

AFC SLD

Last, but not least, we have used a $1300nm$ SLD, between the Giga SLD breakdown and the delivery of the Superlum SLD, but no characterising measurements have been recorded. The advantage with this diode is that it has an output power of $24mW$ whereas the other two delivers around $1mW$ of power each.

The datasheet for this diode specifies the FWHM of the spectrum to be $60.4nm$ which is very similar to the Superlum diode. The coherence length as defined in equation (9) is calculated to $12.9\mu m$. The spectrum for the AFC source is also given in the manual and can be seen in figure 15.

Summary

The different sources each have their advantages. The Giga SLD has one distinguishing feature, it is inexpensive to produce. The SLD was a prototype borrowed by Risø to test and characterize. The spectral characteristics is reasonably good although the oscillatory deviations from a true Gaussian spectrum caused side lobes to appear in the FFT. Also the spectral linewidth of $20nm$ is quite a lot smaller than the Superlum and AFC SLD with a linewidth of $60nm$.

This leads us to the Superlum SLD. This SLD is a commercial product and this shows in the spectral characteristics. The spectrum is almost completely smooth and side lobes are not observed in practise. The linewidth of this source is greater than for the Giga SLD by a factor of three: approximately $60nm$.

The powers of the two SLDs were in both cases close to $1mW$. This is where the AFC SLD is different, since it has an output power of $24mW$. The AFC SLD has a quite smooth spectrum, easily comparable to the Superlum diode.

The Giga SLD seems very promising for use in OCT, because of it's low price and simplicity. One should however be aware of the possible problems with sidelobes.

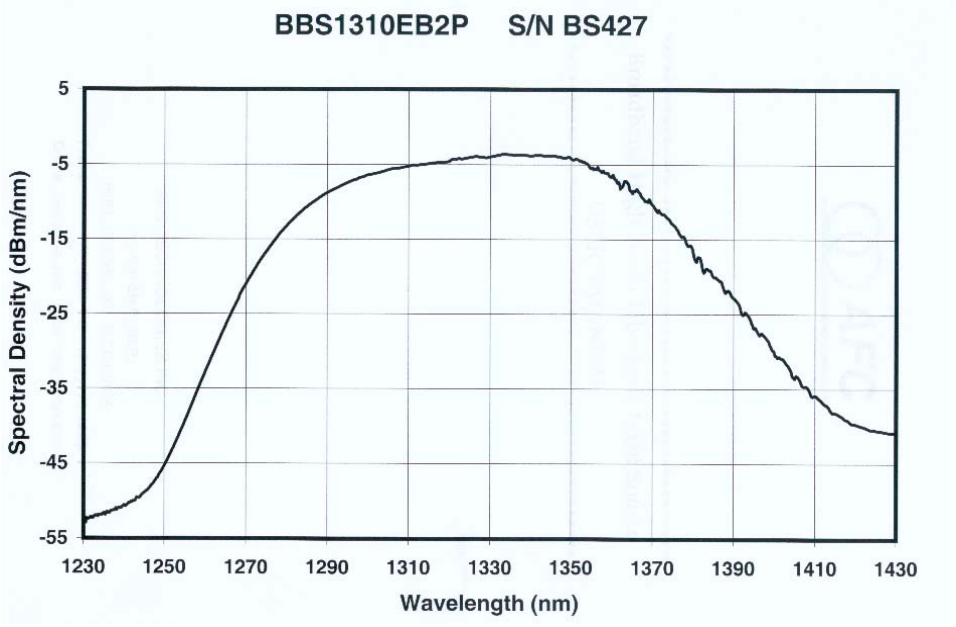

Figure 15. The spectrum of the AFC BBS1310 source.

5 Experimental measurements

5.1 Setup

This section will expand on the description of the OCT system as presented in section 2, by separating the system in 5 parts, each of which will be discussed in the next sections. The partitioning divides the system into: the source, the detector, the reference, the sample and finally the fiber-coupler setup treated as a single "black-box" arrangement. The entire system is built on an optical table to dampen vibrations during measurements.

Source

As discussed earlier, several sources have been used throughout the project. To summarize, the following SLDs have been used: Giga 1540nm SLD, a Superlum 1545nm SLD and a AFC 1300nm SLD. All these sources have been examined earlier.

None of the sources used are overly sensitive to feedback from the system, and consequently no optical isolator was required to be added to the system. This is not to say that the system would not benefit from an isolator, but since using one brings the problem of adjusting the fibers to correct for the extra length, none was used.

Detector

The detector used is produced by the company New Focus and is a multi-purpose detector usable in both a balanced and unbalanced system. The detector consists of two photodiodes which the input fibers are connected directly to, as well as an amplifier circuit.

The conversion from a balanced to an unbalanced detector is done by turning a knob on the top of the detector. This, of course, assumes that the system itself is configured as either balanced or unbalanced.

When the detector is in auto-balanced mode, it uses automatic gain-compensation in the photodiodes to obtain almost perfect intensity noise suppression [12]. This

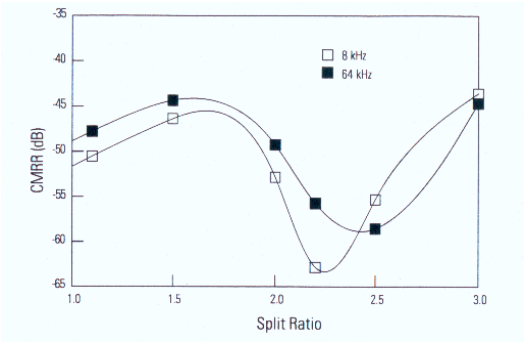

Figure 16. Common-mode rejection ratio versus the split ratio P_{ref}/P_{sig}. From the detector manual, [12]. As shown in this section, the measured signal was modulated at 7-8kHz, so the 8kHz curve should be applicable.

gain-compensation is optimal when the power P_{ref} on the "Ref" input port is ideally twice the power P_{sig} on the "Signal" input port. It is recommended to attenuate the signal if necessary, to achieve this. Unfortunately, no $3dB$ attenuator was available for $1500nm$, so measurements were made without and with a $3dB$ attenuator for $1300nm$ light instead. The attenuator was measured to attenuate $1500nm$ light by $4.5dB$.

When no attenuator was used, the fibers were connected to the input ports so that the ratio P_{ref}/P_{sig} was measured to 0.87. As seen on figure 16, this should give better noise rejection than if the fibers on the input ports were switched, since that would give a split ratio of $1/0.87 = 1.15$, assuming that the slope of the curve doesn't change when the ratio is slightly lower than 1. When the attenuator was used, it was placed on the "Signal" port, so that the split ratio became 2.47, which should give an almost optimal noise rejection.

Reference

The reference constists of a mirror mounted on a scanner. The scanner used here is capable of scanning approximately $5cm$ in μm-steps with a resolution of $50nm$ and a velocity of $6mm/s$. When using the scanner in a repeating fashion, it returns to the same starting position with an accuracy of $\pm 1\mu m$ [17]. The scanner is controlled by a program made in LabView, by Lars Thrane, and can be set to single or multiple scans.

The mirror chosen is based on the source wavelength, so that the mirror correctly reflects light at $1550nm$. In this system silver mirrors were used.

Sample

The sample is whatever one chooses to measure, but the setup around the sample is the same each time. The sample itself is placed in a container - consisting of a cuvette taped to a standard holder for optical tables. The sample fiber is mounted on two scanners (of the same type as the one used in the reference), that can move in one axial and one transverse direction, although only the transverse movement is actually used in a measurement. In front of the sample fiber a lens is placed with a focal length of $16mm$.

Again the scanner responsible for the actual scanning is controlled by a LabView program (also the same as before) whereas the second scanner mentioned is only used to adjust the focal plane of the lens to coincide with the sample.

Fiber setup

The balanced and unbalanced systems uses two different designs and both systems will be described in the following. Some considerations regarding the systems are the same such as the use of collimators in the reference and sample arms, and the use of 50/50 couplers.

The unbalanced system is a simple Michelson interferometer made by a single 50/50 fiber-coupler. The reasoning behind the choice of the 50/50 coupler is mentioned in section 3.2, and the system can be seen in figure 5.

The balanced system uses four couplers (figure 7) each of which is 50/50. This design ensures that the optical path lengths in the reference and sample arms are the same - if the fibers on the couplers are equally long. The last coupler leads to the detector and ideally a $3dB$ attenuator should be connected between this coupler and the detector.

Data acquisition

The data acquisition is not part of the OCT system per se, since it is an integral part in all experimental setups. For this system the signal coming from the detector is passed through a combined amplifier and filter to a digitizer in the form of a A/D card connected to a computer.

The filter contains a low pass and high pass filter where each can be connected independent of the other. The limits of the resulting band pass filter was chosen to be from $3kHz$ to $13kHz$ based on the frequency generated by the moving scanner.

The signal has been shown to vary as $cos(k_0\Delta l)$, eqn. (7). The path difference Δl is given by $2vt$, where v is the scanner velocity and t is the time, since the light has to move to and from the reference mirror. This gives

$$cos(k_0\Delta l) = cos\left(\frac{2\pi}{\lambda_0}2vt\right)$$

Comparing this to the general expression $cos(2\pi ft)$, where f is the frequency modulation, we obtain

$$f = \frac{2v}{\lambda_0} = \frac{2 \cdot 6mm/s}{1545nm} = 7.8kHz$$

The A/D card has a number of different settings accessible through the LabView program run on the pc. The settings in turn control the resolution of the digitized signal so that a resonable value for the limits must be chosen with caution. The digital signal is then used as input for the LabView program mentioned earlier, where the data can be saved for later study.

5.2 Noise and SNR, measurements and calculations

In this section we determine the noise through experimental measurements, and construct a simple noise model from these experimental measurements. We further discuss the noise sources that limit the system.

Spectrum of a signal measurement

To begin the inspection of the noise in the OCT system an FFT of the signal in figure 3 has been done, although now the entire measurement has been used where figure 3 only shows a small portion. The result is the spectrum of the noise and can be seen in figure 17.

This plot shows several interesting phenomena. Firstly, the pass band region of the filter is clearly visible, although the band is somewhat larger than the limits chosen (3-13kHz) and the noise at the edges of the band is also larger than the noise in the middle of the band. This structure must be an effect of the type of window used in the filter. The signal is seen as the peak at approximately $7kHz$ and is very small, since the signal is weak and only constitutes a small portion of the Fourier transformed data. The last detail one should notice in the plot is the large peak close to zero, which a closer examination shows to be $50Hz$ noise

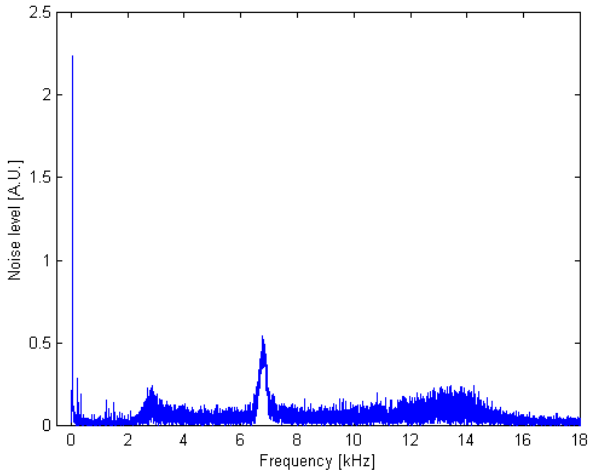

Figure 17. This plot shows the spectrum of the noise in kHz. The pass band of the filter is visible in the region from 3-14kHz, as well as the signal at approx. 7kHz. The large peak is at 50Hz and is very prominant.

(the DC offset is already subtracted). This $50Hz$ contribution is quite large when compared to the the rest of the noise spectrum which seems to be more or less "white", in the sense that it is frequency independent.

Noise Determination

We wish to determine the optimal system parameters, such as the coupler split ratio and reference reflectivity. Therefore a model is needed to determine both the signal and the noise for different parameters. Equations (13) and (14) allow determination of the signal for different parameters, because the powers P_s and P_r are given by the equations in section 3. The noise however, will be shown to deviate much from the theoretical expressions, and we therefore determine the noise experimentally for different levels of the DC photocurrent. The expected DC photocurrent can be determined from the system parameters, $I_{dc} = \rho(P_r + P_x)$, as an expression for P_x is also found in section 3, and from this value of I_{dc} the noise can be evaluated for any choice of parameters.

As mentioned in section 3.1, when considering the SNR, the interesting property is the contrast. Hence, the noise is calculated from the "noise floor", where no interference signal is detected.

The two setups used are the unbalanced system in figure 5, and the balanced with four beamsplitters, figure 7. The balanced system with 4 beamsplitters was used instead of the system with 3 beamsplitters (figure 6), because we did not have fibers available with appropriate lengths for achieving the correct optical path length. The balanced system with 4 beamsplitters obviously looses more power, than the system with 3 beamsplitters, as can be seen from the figures mentioned, because light is coupled out of the system at the power measurement ports. The SNR is therefore lower.

The setup is built as described in section 5.1, with the exception, that a mirror is used in the sample arm. This choice is made to obtain a simple interference signal (as opposed to a medium with multiple-layers where several interference signals occur), the reflectivity is known and greater signal power is obtained. When considering the result it should, for that reason, be born in mind, that the SNR will be considerably larger than the corresponding result for a biological sample.

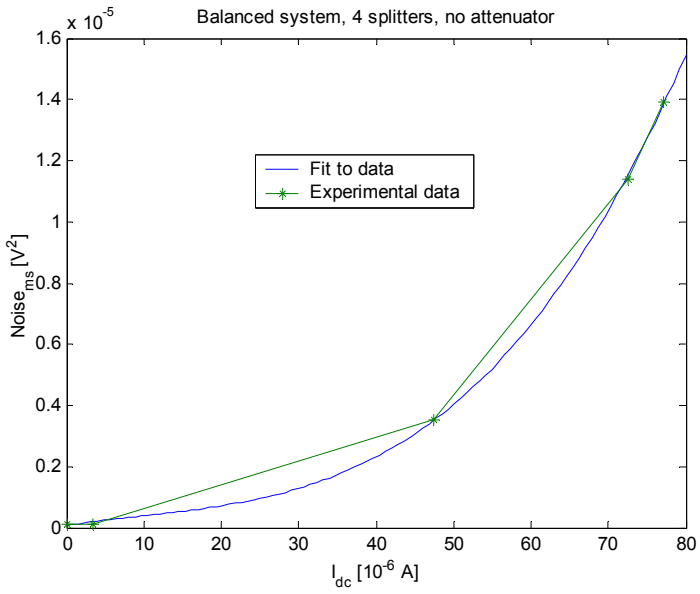

Figure 18. The experimental measurements and the 3rd degree polynomial fit for the balanced system with 4 beam splitters, no attenuator and 20dB amplification of the measured signal. This is used to estimate the noise as a function of the mean photocurrent I_{dc}. The noise variance is fitted with $\sigma_v^2 = aI_{dc}^3 + bI_{dc}^2 + cI_{dc} + d$, where $a = 3.70 \cdot 10^{-11}$, $b = -1.04 \cdot 10^{-9}$, $c = 3.83 \cdot 10^{-8}$ and $d = 7.34 \cdot 10^{-8}$.

A measurement of the noise is done simply by making a data acquisition from LabView of the output signal, when the optical path difference is much larger than the coherence length, so that the interference signal is not observed. The highest possible resolution of the A/D card is used. The noise is then calculated using Matlab to find the variance from the data set, after the mean offset has been subtracted (there is a small DC offset in the raw data). To measure the maximum of the signal, the interference signal has to be detected. The data acquisition is performed 20 times in order to get a mean value of the maximum. Again, Matlab is employed to calculate the mean signal-maximum.

To see how the noise changes with the DC photocurrent, the above mentioned measurements are performed at different values of the SLD current. To find the corresponding DC photocurrent, the power P_{dc} at the detector is measured with a powermeter at the same SLD currents, and the photocurrent is calculated by assuming that photocurrent is $I_{dc} = \rho P_{dc}$ for the unbalanced case and $I_{dc} = \rho(P_{dc,ref} + P_{dc,sig})$ for the balanced case, where $P_{dc,ref}$ and $P_{dc,sig}$ are the powers measured at the "Ref" and the "Signal" detector ports respectively.

Modeling the noise

Two methods are used to model the noise versus DC photocurrent. The *theoretical model* is based on the calculations in section 3. The *experimental model* uses a 3rd degree polynomium to estimate the noise as a function of the mean detector photocurrent by fitting the data acquired from the measurements, see figure 18.

Notice that, when the term 'experimental model' is used, the signal is still calculated with equations (13) and (14), but now the noise is estimated using the fitted polynomials. *Measurements* are made for an unbalanced system with the amplifier set to $0dB$ and for a balanced system with the amplifier set to 0, 10 and $20dB$ respectively, with and without an attenuator on the detector "Signal" port.

Since the theoretical model calculates the noise in ampere and the noise is measured in volts, the theoretically calculated noise has to be converted to volts.

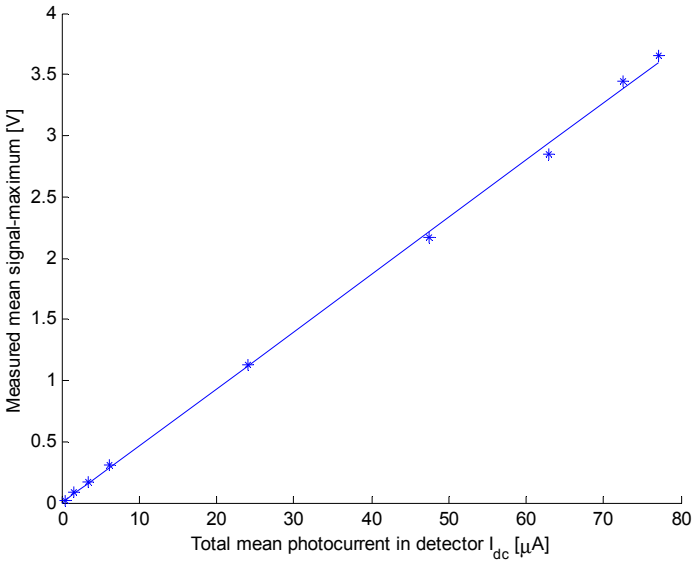

Figure 19. The measured mean signal-maximum $V_{s,\max}$ versus the calculated mean photocurrent I_{dc} in the detector, for the case of balanced detection without an attenuator, and without amplification. A fit to the experimental points is shown, and from the slope of this fit the conversion factor is found to be $0.0467 \cdot 10^6 V/A$.

For this reason a plot is made of the measured interference signal-maximum in volts versus the dc photocurrent. From a linear regression the slope is derived and directly used as a conversion factor since $I_{dc} = I_{s,\max}$.

This can be seen from the following: The interference signal-maximum is given by $I_P = I_1 + I_2 + 2\sqrt{I_1 I_2}$, the filter removes the DC component $I_1 + I_2$, so that only the interference term $2\sqrt{I_1 I_2} = 2I$ is recorded in LabView, assuming that $I_1 = I_2 = I$ when two mirrors are used. The powermeter only measures the DC term (since the OPD is greater that the coherence length), which then becomes $I_1 + I_2 = 2I$. The measured signal-maximum should therefore correspond to the measured power, which can be converted to a photocurrent in the detector.

The conversion factor was found to increase by 10 and $20dB$ respectively, when these amplifications were used, as expected. The conversion factor was also found to be different for unbalanced detection, balanced detection without an attenuator and for balanced detection with an attenuator. This is probably because the internal detector gain is dependent on whether it is set for balanced or unbalanced detection, and dependent of the ratio between the power on the "Signal" and the "Ref" input port. The conversion factors are shown in Appendix B.

When using the model, the following limitations should be kept in mind.

The experimental measurements are made with two mirrors, which makes the beat noise proportional to $P_r P_x \approx I_{dc}^2/4$. When the experimental model is used on a balanced system and the sample reflectivity is much lower than the reference reflectivity, the beat noise is over-estimated since now $P_r P_x \ll I_{dc}^2$, giving a lower beat noise than if two mirrors were used. The fitted polynomials therefore give the best estimate for the noise when the sample and reference reflectivities are equal.

These noise measurements are system specific: we determine the noise added anywhere between the detector and the computer. The contributions from the different components (detector, amplifier, filter, A/D converter, etc.) are all lumped together, to determine the noise for the specific system at hand. This is not a very general method, but could be used when one seeks to use more optimal beamsplitters or attenuation of the reference power. For a general theoretical treatment, see [14].

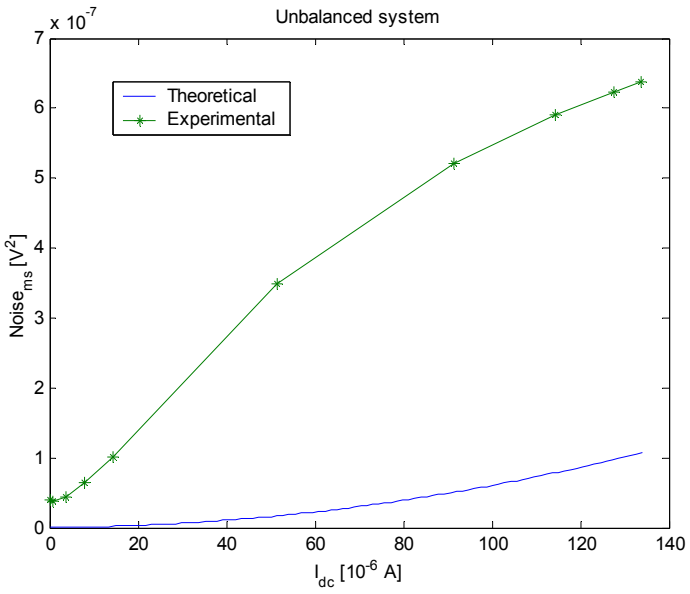

Figure 20. Plot of noise versus DC photocurrent for an unbalanced system using the theoretical model and the experimental data. The asterixes are experimental values. The experimental curve has a larger offset and experiences a larger increase with the photocurrent, than the curve based on theoretical calculations.

Finally, when deriving equation (5), it was assumed that the interfering light beams have the same polarization, but in the experiments unpolarized light was used. However, this should only change the results slightly.

Default choice of parameters in the models: $\Delta\lambda_{FWHM} = 62nm$, $\lambda_0 = 1545nm$, $B = 10kHz$ and $V = 0$. When nothing else is stated, an input noise current (INC) of $3pA/\sqrt{Hz}$ has been assumed for the theoretical model. The data points are connected by straight lines for ease of comparison. The matlab code can be seen in Appendix C.

Unbalanced system In figure 20 a linear plot of the noise versus the DC photocurrent is shown without amplification. The offset of the theoretical plot, caused by reciever noise, is negligible and can not be seen in the figure. Since the noise is proportional to the square of the mean detector photocurrent $\sigma^2_{theoretical} \propto I_{dc} + I^2_{dc}$, the graph has the form of a parabola. The plot of the experimental measurements, however, does not have the same shape, it has a larger offset and a negative curvature. The larger offset indicates that the intensity-independent noise is larger than the receiver noise used in the theoretical model, this could be caused by the internal detector amplification of the receiver noise and addition of noise not included in the theoretical model as discussed in the section below.

Figure 21 shows again the noise versus DC photocurrent, but now on a semilog scale. The two plots now show a uniform behavior. The reason for this seems to be that a constant multiplicative factor of the noise has been left out of the theoretical model, possibly coming from the internal detector gain.

To closer examine the observations from before the theoretical plot in figure 22 has been multiplied by a factor 2.4^2 and a constant of $3.65{\cdot}10^{-8}V^2$ has been added. This gives a somewhat reasonable match with the experimental measurements.

Balanced system Figure 23 shows the noise versus the DC photocurrent for a balanced system on a log scale. The $10dB$ difference between the experimental curves are observed for large I_{dc}. However, for low I_{dc}, it is seen that the $10dB$ curve and the $0dB$ curve flattens out at a certain value, approx. $3\text{-}4{\cdot}10^{-8}V^2$.

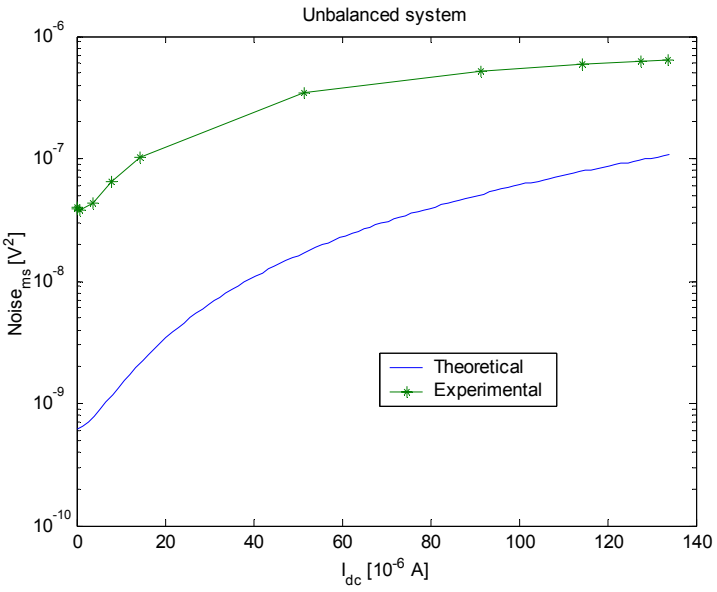

Figure 21. The same plot as the previous figure, but on a semilog scale.

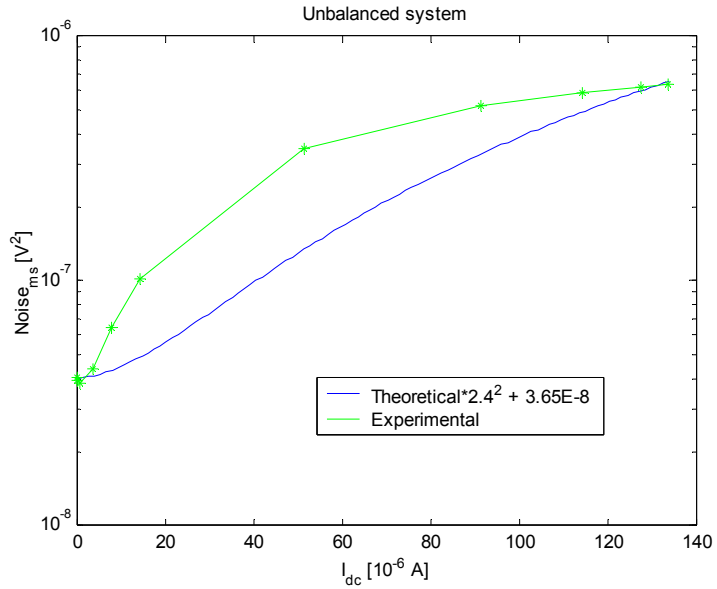

Figure 22. The experimentally measured noise and the theoretically calculated noise modified by multiplication and addition of an intensity-independent term, for an unbalanced system.

This indicates that there is an additional noise which is not amplified, i.e. the noise is added after the amplifier. This could be $50Hz$ noise picked up in cables, connections or the A/D card. The $50Hz$ noise is known to be present in the system, see figures 3 and 17, and was observed even after filtering supporting the postulate that the noise is added after filtering. This $50Hz$ noise could also arise if not all components have a common ground, [8].

Again the theoretical noise is lower than the measured noise and except from the change caused by the noise after amplification the shape is the same. The theoretical noise is multiplied with a constant and added with the minimum noise from the noise measurements, and the resulting plot is seen in figure 24. When an attenuator is used, the result shown in figure 25 is obtained (for more figures

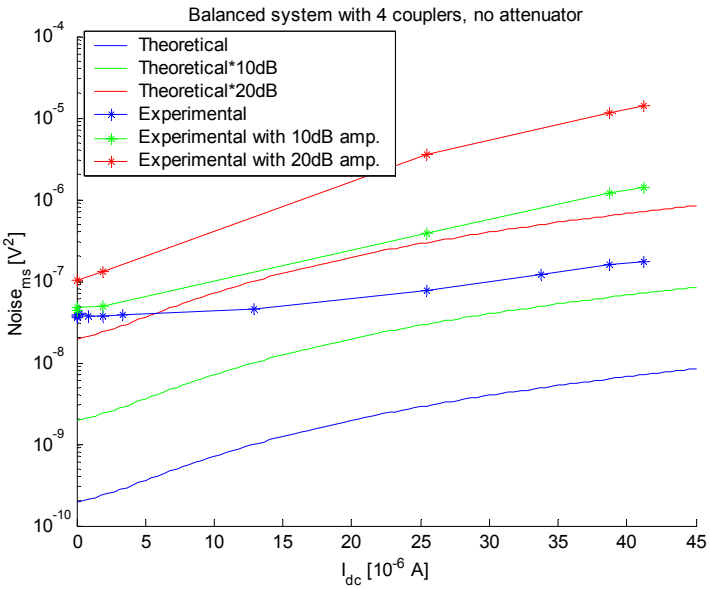

Figure 23. The noise measured at 3 different amplifier settings for the balanced system without an attenuator, with the theoretically calculated noise, multiplied by 1, 10 and 100 for simulation of amplification.

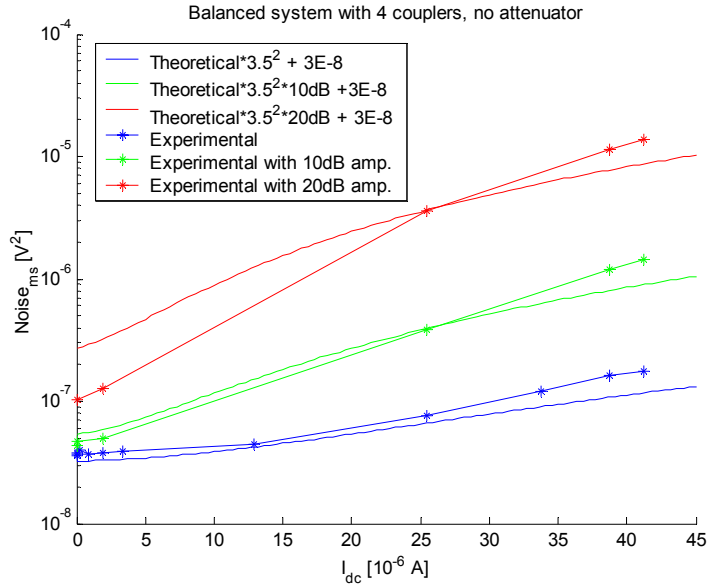

Figure 24. The same plot as before, but now the theoretical noise has been modified by multiplication and addition of an intensity-independent term, to show that internal detector gain and a post-filter noise addition could explain the difference between the theory and experiment.

with attenuator see Appendix A). The modified theoretical model seems to fit quite well to the experimental measurement in both cases. This supports the presumption, that the noise is amplified in the detector and that an additional noise is added after amplification/filtering. It is seen that the noise level is lower, when an attenuator is used.

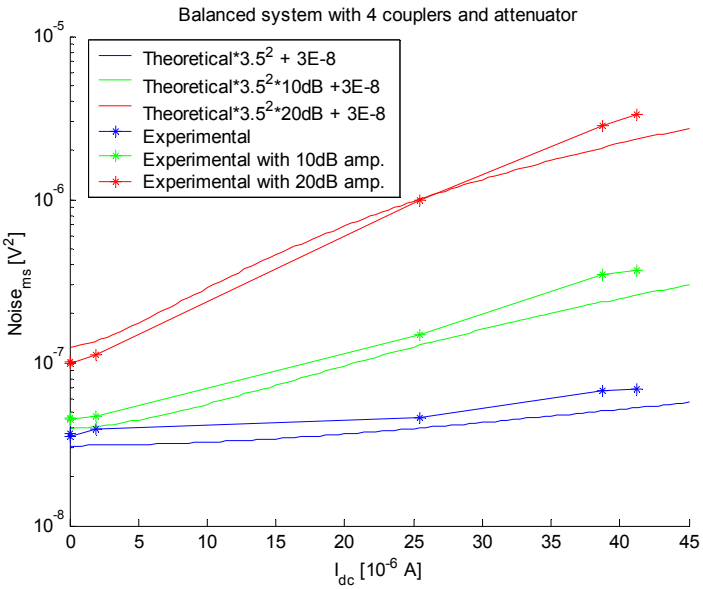

Figure 25. Again the same plot as before, but now an attenuator is used in the balanced system with four couplers.

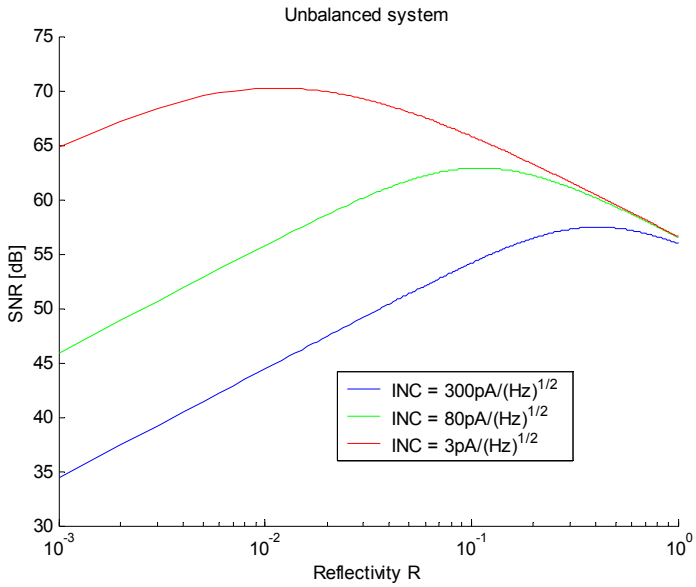

Figure 26. SNR (dB) versus reflectivity for different values of input noise current ($pA/\sqrt{Hz}$), obtained using the theoretical model. It is readily seen that the optimal reflectivity decreases as the INC decreases. P_{so} is set to $1mW$, $\Gamma_s = 0.0001$, $\Gamma_x = 0.01$, and the coupler split ratio K is set to $1/2$.

Modeling of SNR versus splitting ratios and reflectivity

A theoretical model of SNR versus splitting ratios is made from the theoretical expression as was done in the noise modeling. Now the splitting ratio of interest is varied from 0.01 to 0.99, and for each of these values the powers P_r, P_s, P_x are calculated. Using expressions for mean-square photocurrent and noise the SNR is calculated

In figure 26 a plot of the SNR versus the reflectivity is shown for different values of the input noise current (INC) . The theoretical model is used. It is seen that the maximum SNR is reached at lower reflectivities, when the INC is decreased. For INC $= 300pA/\sqrt{Hz}$ the maximum is reached at a reflectivity close to 0.4. For

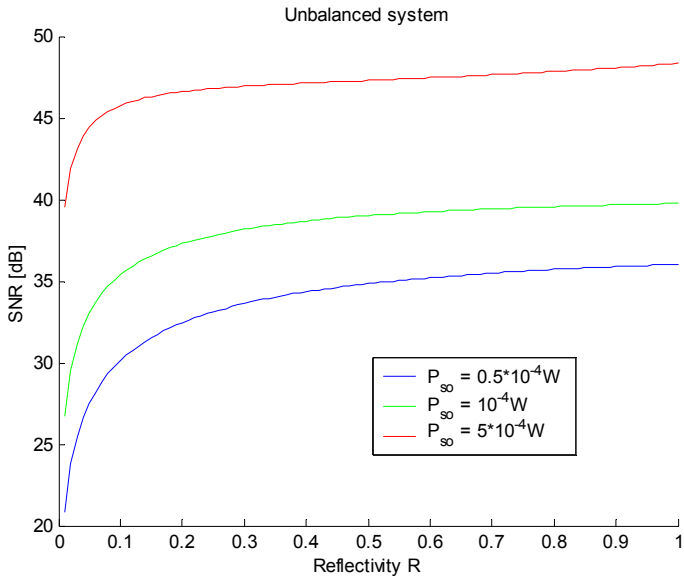

Figure 27. SNR versus reflectivity R for different values of source power P_{so}, obtained using the experimental model. The SNR increases monotonically with the reflectivity, indicating a large noise floor. $\Gamma_s = 0.0001$, $\Gamma_x = 0.01$, and the coupler split ratio K is set to $1/2$.

INC $= 3pA/\sqrt{Hz}$ the optimum reflectivity is close to 10^{-2}, indicating that the maximum moves asymptotically towards zero. This means that, when the noise in the detector is very low, the reference signal should be attenuated. On the other hand, when the detector noise is high, the signal from the reference should be as large as possible. The reason, why attenuation of the reference is advantageous, is that the shot noise and excess intensity noise is reduced. So, if the intensity-independent noise is not negligible, there is no pay off in attenuating the reference power.

The same situation is shown in figure 27, where the experimental model is used. The three plots is made for different values of the source power. As expected the SNR increases with the source power. However, Podoleanu [14] has shown, that there is a maximum limit for the source power above which the SNR does not increase further. This is not seen in the mentioned plot, since a further increase in the source power, would give a theoretical mean photocurrent I_{dc} greater than measured experimentally, and would thus force us to extrapolate beyond the data points, and we have chosen to focus on the actual attainable limits with the given system. The deviation between the theoretical and the measured I_{dc} can be accounted for by losses in e.g. fiber connections and couplers. It is seen that the SNR increases monotonically, when the reflectivity is increased. The reason to this must be that there is a larger noise floor than the input current noise given in the detector manual [12]. This corresponds to the discussion in the previous section, where the noise floor is estimated to be $3.65 \cdot 10^{-8} V^2$.

Corresponding 3D plots of figure 29 can be seen in figures 44, 45 and 46 in Appendix A.

A plot of the SNR versus K_1, for different values of input noise current, using the theoretical model is shown in figure 28. It is seen that the maximum SNR occurs for higher values of K_1, when the noise in the detector is lowered. This is further explained below.

The influence of the splitting ratio of the first coupler is examined in figure 29. The graph shows the SNR as a function of the splitting ratio and different amplifier settings. When the splitting ratio, $K_1 = 0$ all the light goes to the reference arm,

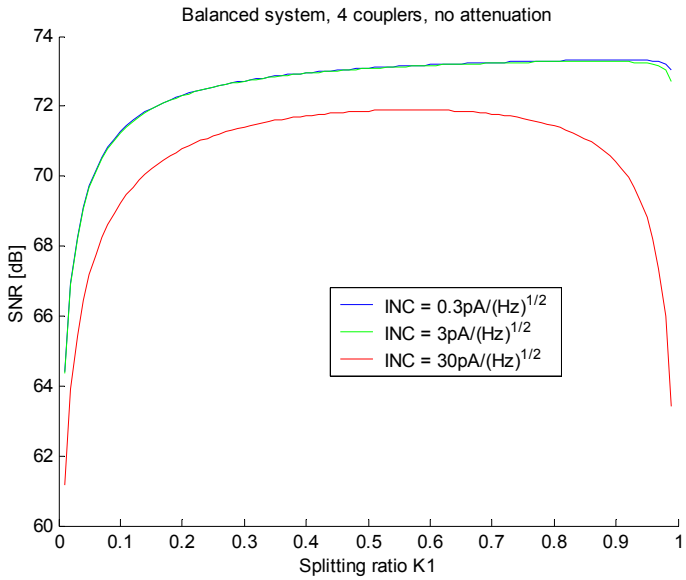

Figure 28. SNR versus coupler splitting ratio K_1 with 3 different receiver input noise currents, for a balanced system with four couplers and no attenuator. P_{so} is set to $1mW$, $R = 0.9$, $\Gamma_s = 0.0001$, $\Gamma_x = 0.01$, and the coupler split ratios K_2 and K_3 are set to $1/2$.

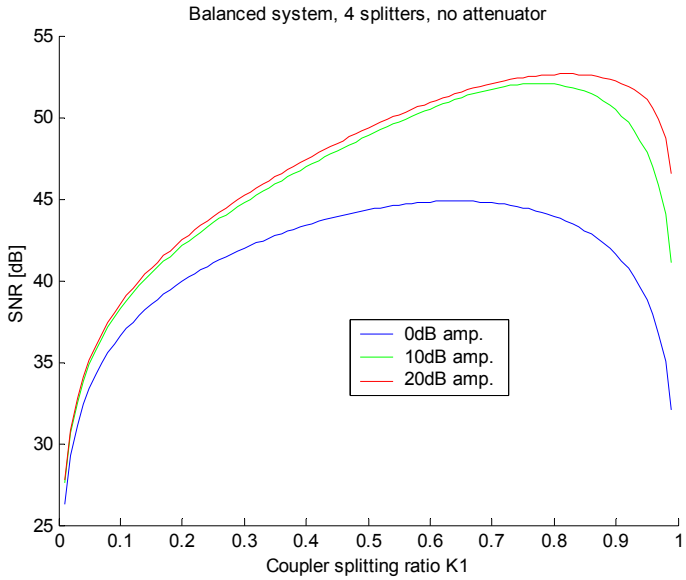

Figure 29. SNR versus coupler splitting ratio K_1 with 0, 10 and 20dB amplification, for a balanced system with four couplers and no attenuator. P_{so} is set to $0.4mW$, $R = 0.7$, $\Gamma_s = 0.0001$, $\Gamma_x = 0.01$, and all the coupler split ratios $K2$ and $K3$ are set to $1/2$.

whereas a value of 1 means that all the light impinges on the sample. It is observed that the SNR is maximized at $K_1 = 0.65$, with no amplification of the signal. When the signal is amplified the optimal splitting ratio for K_1 nearly reaches 0.8 with $10dB$ amplification and just exceeds 0.8, when the signal is amplified $20dB$. This leads to the same conclusion as in the theoretical plot (figure 28): when the intensity-independent noise is negligible, it is advantageous to send more light to the sample (which has a lower reflectivity than the reference), since this gives less intensity-dependent noise. This means that the effect of amplifying the

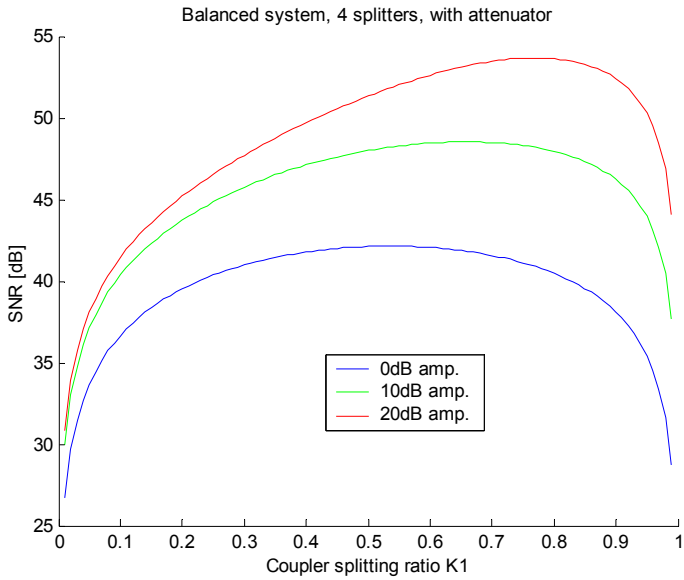

Figure 30. For 0dB, 10dB and 20dB the optimal split ratios and corresponding SNR are respectively: $K_1 = 0.53$ *giving* $SNR = 42dB$, $K_1 = 0.66$ *giving* $SNR = 49dB$ *and* $K_1 = 0.77$ *giving* $SNR = 54dB$.

measured signal is to lift the signal above the noisefloor, making it insensitive to the small noise added somewhere after amplification/filtering. As seen in figure 23, the intensity-independent noise is dominating (for small values of I_{dc}) when the signal is not amplified. For small intensities the noise is therefore approximately constant and since the signal is proportional to $P_r \cdot P_s \propto (1 - K_1) \cdot K_1$ the SNR maximizes when the splitting ratio K_1 is close to 0.5. As the signal is amplified the shot noise will be more dominating and the optimal splitting ratio should therefore approach the theoretical value: $K_1 = 0.87$ (figure 43 in Appendix A). It is seen that the SNR improves significantly from 0 to $10dB$ amplification ($7-8dB$ SNR improvement at the maximum), but from 10 to $20dB$ amplification, only a small improvement in SNR is observed.

In figure 30 the same plot is shown, for the case when an attenuator is added to the system. Here it is interesting to notice that although the detector should give better noise rejection when an attenuator is used, and the noise indeed was measured to be smaller (figure 25), this is not sufficient to compensate for the attenuation of the signal, since the SNR is seen to be lower than when no attenuator is used. This is because the noise added after the amplification/filitering is still present (the "noisefloor") and dominates for low intensities, thereby burying the improved noise rejection of the detector. However, when $20dB$ amplification is used, the detector noise is lifted above this noisefloor, and the signal is no longer limited by the noisefloor. Therefore when 0 and $10dB$ amplification is used, the SNR is lower when an attenuator is used, but is slightly better when $20dB$ amplification is used, compared to the same amplifications without an attenuator.

Modeling of SNR versus mean photocurrent

The mean signal maximum was measured experimentally and so an experimental value for the SNR can be determined. The plot in figure 31 shows that using the experimental model gives a much better agreement with experimental data than the theoretical model, as expected. It seems that the signal is determined reasonably when calculated with equation (13). The plot shows the SNR increases with the mean photocurrent I_{dc}, as expected, and seems to approach the theoretical

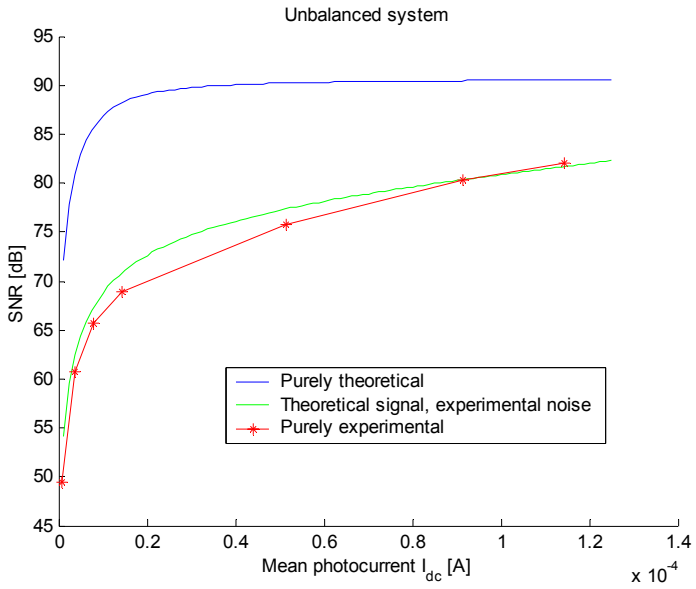

Figure 31. The SNR is calculated with the theoretical and experimental model, and compared with the experimental data. For the theoretical calculations P_{so} is varied from $5\mu W$ to $0.5mW$, $R = \Gamma_s = \Gamma_x = 0.5$, and the coupler split ratio K is set to $1/2$.

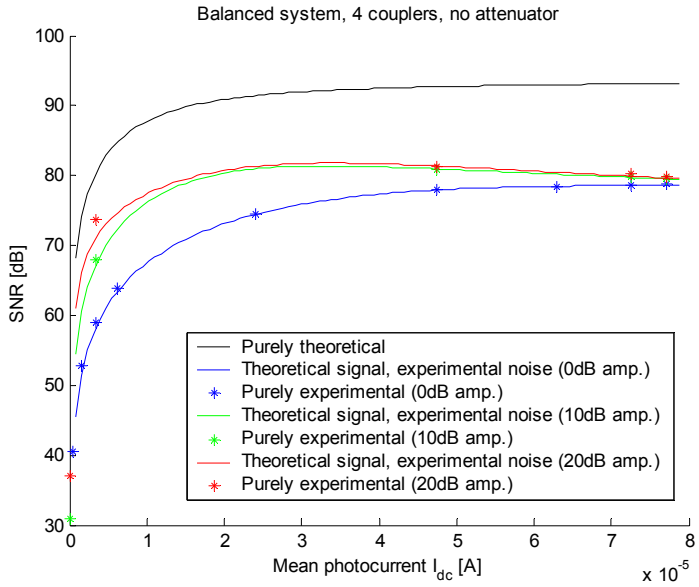

Figure 32. For the theoretical calculations P_{so} is varied from $4.5\mu W$ to $0.45mW$, $R = 0.6$, $\Gamma_s = \Gamma_x = 0.8$, and all the coupler split ratios K_1, K_2 and K_3 are set to $1/2$.

value as the current increases.

The influence of the mean photocurrent I_{dc} on the SNR is show in figure 32, where three values of amplification is applied to the signal. In this plot both the theoretical model, experimental model and measurements are examined. The theoretical and experimental curve is seen to have same form although the magnitude predicted by the theoretical model is to high, due to an under estimation of the noise in the theoretical model. The three series of experimental measurements and the corresponding experimental models all show a good match, both in the form and magnitude. If the signal is not amplified the curve shows a monotone increase

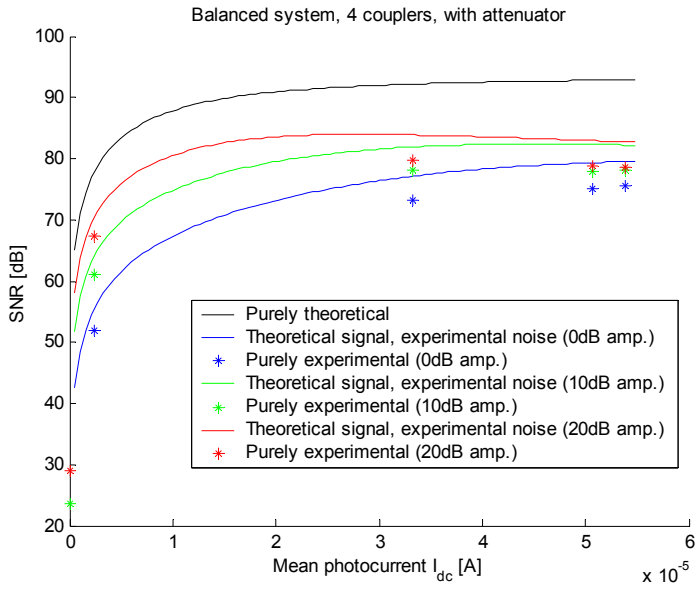

Figure 33. For the theoretical calculations P_{so} is varied from $5.4\mu W$ to $0.54mW$, $R = \Gamma_s = \Gamma_x = 0.6$, and all coupler split ratios $K1, K2$ and $K3$ are set to $1/2$.

in the SNR as the photocurrent increases, but seems to approach a maximum asymptotically, as shown theoretically by Podoleanu [14]. With an amplification of the signal of 10 or $20dB$ the SNR now begins to decrease slightly when I_{dc} reaches a certain threshold ($I_{dc} \simeq 30\mu A$). This is also predicted by the experimental model. Between the curve showing no amplification and the next with $10dB$ amplification there is a proportionally large jump compared with the separation between the 10 and $20dB$ amplification plots, which is the same phenomenon observed in figure 29 and 30 (see discussion of these plots).

For large mean photocurrents the experimental measurements of the SNR are seen to converge at same level, since both the signal and pre-filter noise are amplified equally and the post-filter noise is negligible. At smaller photocurrents the SNR is improved by amplification of the signal, because the post-filter noise will dominate this region.

An attenuator is added to the system and the measurements above is repeated. This gives figure 33, where the theoretical model, experimental model and measurements are compared. The correspondence between the experimental model and the experimental measurements is not as good as in figure 32. This could be caused by the use of different parameters in the experimental model, such as P_{so} and Γ_s, when plotting the figures. The parameters are not the same as in the experiments, since this would give a calculated I_{dc} greater than measured and so extrapolation of the data would be necessary. This may be because calculation of the maximum signal in the SNR does not account for losses in the optical components, and so has been given a too high value in the experimental model. The general shape of the individual plots has not changed with the addition of an attenuator, as of course it should not.

5.3 Imaging of biological tissue

A series of images were made with the 1545 nm OCT system for the unbalanced as well as the balanced setup. The motivation is to examine how suitable a $1.5\mu m$ system is to image biological tissue. Therefore it is very interesting to compare with images made at another wavelength. A permanent setup of a $1.3\mu m$ OCT system was available in the laboratory, and images were made with this system under the

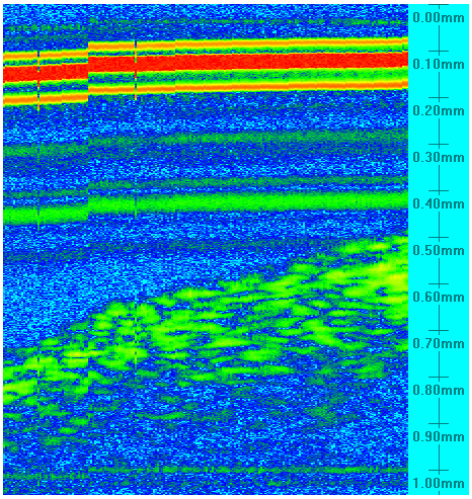

Figure 34. This is what an OCT image generally looks like. The image is color-coded, so that strong reflections are red and weak ones are yellow, green or blue.

same conditions as the $1.5\mu m$ system in order to allow comparison. Images are also made with a different technique, confocal microscopy, for comparison. The following images have a scale on the right side, where a constant refractive index of 1.4 has been assumed for simplicity.

The OCT image

To make an OCT image the setup described in section 5.1 is used. The image is recorded one axial scan at a time, which is done by moving the reference mirror a certain distance and back again. The sample fiber is move laterally and another axial scan is recorded. A typical number of scans is 200, moving the lightbeam e.g. 5 or $10\mu m$ laterally each scan. The raw data from the measurement are saved in binary file format since the amount of data is quite large. A computer program, ViewerSave, was employed to convert the data to a false-color image. The samples used in the measurements are:

- An onion
- A mouse biopsy
- An artery biopsy

An example of an OCT image is shown in figure 34. The colors are interpreted in the following way: red corresponds to a strong signal and as the signal gets weaker the color turns from yellow to green - blue corresponds to the weakest signal. The color-coding uses a logarithmic scale so that smaller signals are emphasized. The images show a cross section of the sample, where the sample-surface is at the top of the image and moving vertically down corresponds to moving deeper into the sample.

As can be seen in most of the images, there is a vertical displacement of some of the scans. This is caused by the scanner, when it does not return to the exact same initial position. These displacements could be corrected by a computer program. However, none of the shown images are corrected, since the primary focus of this project has been to analyse the SNR of the system.

Image of an onion When examining the onion no glass plate was situated in front of the sample. The onion shell was simply attached to a cardboard placed

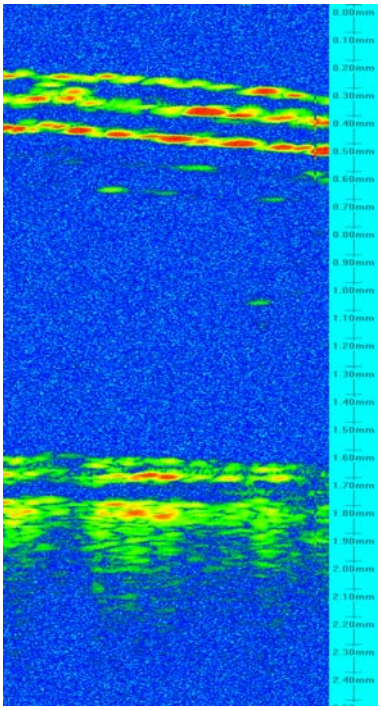

Figure 35. This OCT image show a thin slice of onion attached to a glass capillary which in turn is attached to a piece of cardboard.

vertically. The penetration depth in the images is quite large, about $2mm$ without amplification. The images of the onion as shown here were all made with the $1.5\mu m$ system.

A glass capillary tube is used to obtain a well-known reference in the image. In figure 35 an image, of a very thin layer of onion stuck on a piece of tape, is shown. The tape is attached to the cardboard, with the capillary between the tape and cardboard, perpendicular to the lateral scan direction. The onion is seen in the top of the image ($0.3mm$). Further down the front wall of the capillary is seen at $0.4mm$ and $0.5mm$, since both the front and back edge of the wall give reflections. The structures at $1.6mm$ and $1.8mm$ may be the back walls of the glass and the cardboard. As seen, OCT images can be difficult to decipher. The image covers a lateral distance of 1mm, with 200 depth-scans each separated by $5\mu m$.

In figure 36 the capillary is pushed into a larger piece of onion and again placed perpendicular to the scan direction. The capillary is seen in the right side of the picture as two parallel yellow lines (approximately 0.6 and 0.7mm into the sample), which corresponds to the beginning and end of the glass capillary. It is even possible to see the curvature of the capillary.

Again the image is 1mm across and the interesting features of the image extends to a depth of just under 0.8mm. In both images of the onion each vertical scan line has been copied twice to ease the study of the pictures. Also both images were recorded with an amplification of 20dB.

Comparison between 1.3 and 1.5 μm systems

Mouse biopsy In figure 37 two images of a mouse biopsy is shown. The images are made with the same power impinging the samples, but with different wavelengths, and the color codes are the same for both images. The measurements are made without moving the sample, and both uses 200 scans with a spacing of

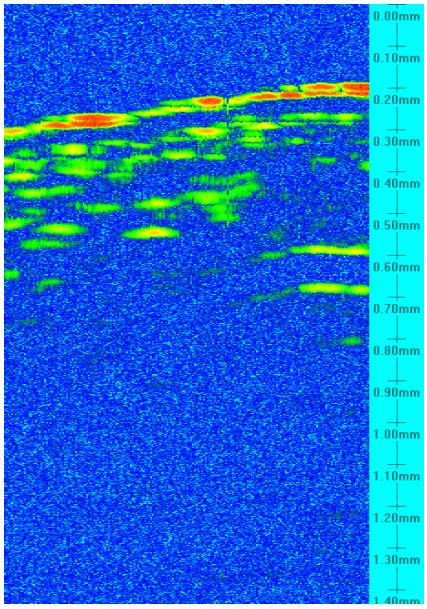

Figure 36. A glass capillary inserted into a piece of onion. This image was made with the unbalanced setup and the 1545nm Superlum source.

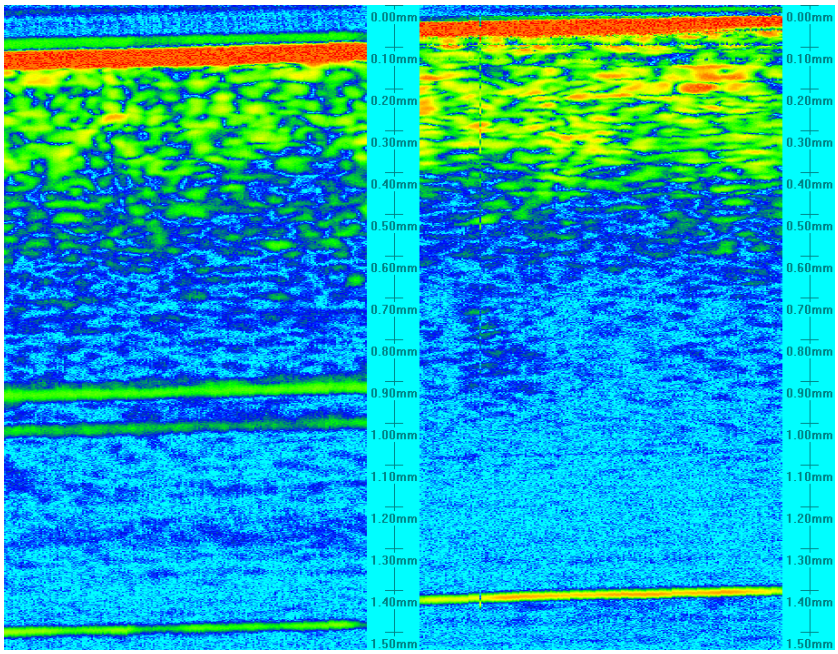

Figure 37. Two OCT images of a mouse biopsy. Left: The image is recorded using the 1300nm AFC source. Right: This image is recorded using the 1545nm Superlum source. Both samples cover a lateral distance of 1mm (or 2mm)

$5\mu m$ to cover 1mm of the sample (lateral distance). The signal was amplified by 20dB before it passed the filter.

To change from one system to the other the collimators at the sample arm and the reference arm is replaced. Hence, the two measurements are probably not made at excactly the same spot on the sample, and the sample collimator may be slightly differently placed with respect to the lens. The biopsy is taken

from the skin on the belly of a white mouse and the images are seen to be quite homogeneous.

The red border at the top stems from the glass surface. It is possible to see about 1 mm into the sample. The thin line deep into the picture stems from a side lobe of the glass surface, or unwanted internal reflections in the system. The two lines which are only in the $1.3\mu m$ system are most likely ghosts from undesired reflection inside the system.

The main feature of these images is a very uniform layer just beneath the glass surface. This layer extends to a depth of approximately 0.9mm in the $1300nm$ image and $0.7mm$ in the $1545nm$ image, and looks qualitatively similar in the two images, although the individual blops in the layer mentioned are generally larger and more separated in the 1300nm image than in the $1545nm$ one. However the penetration depth seems to be similar for both systems, taking the vertical alignment of the two images into account, with a slightly larger depth in the $1300nm$ image.

It was expected beforehand that the $1545nm$ system would have a larger penetration depth than the $1300nm$ system, which is due to the decrease in the scattering of light at higher wavelengths. This is not observed in the two images, but may be caused by a slight misalignent of the sample collimator, as this was replaced when making the $1545nm$ image.

Artery biopsy The next set of images (fig. 38) a biopsy on an artery is shown. As before the power of the sources has be adjusted so the light reaching the sample has the same intensity in both cases. The first image was done using the $1300nm$ source while the second one uses the $1545nm$ source, although for both images the fiber-system were the same, i.e. when changing from 1.3 to $1.5\mu m$ systems *only* the source were changed. This way of changing the wavelength means that the system itself is handled as little as possible, so that the sample should be imaged at exactly the same place.

As with the mouse biopsy there are a red line in the top of both images coming from the glass-tissue junction. On both sides (top and bottom) of this red line a thinner, lighter line is seen. These lines are most likely side lobes from the glass-tissue junction. Further in the sample (0.9, 1.0 and $1.5mm$ in the left image and 0.4, 1.0 and $1.5mm$ in the right image) several more lines are seen, which as before could be side lobes from other reflections in the tissue, or they could be ghosts from the system itself.

The sample can be seen to slope downwards from right to left in both images, and it can be seen to be distanced slightly away from the glass surface (at a depth of $0.7mm$ in average). This means that the sample was not in contact with the glass surface during the measurement and that it has been placed at an angle in respect to the glass.

In the middle of the picture (vertical distance), where the sample is seen, the intensity of the reflections from the $1300nm$ system is quite a lot stronger than the ones from the $1545nm$ system. This is due to the setup of the measurement, where both sources were coupled to the same fibers. This means that the light from the $1545nm$ source propagated through fibers designed for $1300nm$ light. This may have caused some attenuation of the light from the $1545nm$ source. It was also known that the $1300nm$ $3dB$ attenuator at the balanced detector, causes a $4.5dB$ attenuation of the $1500nm$ light, thus reducing the possibility of a direct comparison of the two images.

As before only one layer of tissue can be seen, which means that the artery imaged is homogeneous down to 1.2-$1.3\mu m$ as seen in the left image of figure 38. The remarks about penetration depth from the previous section should also be

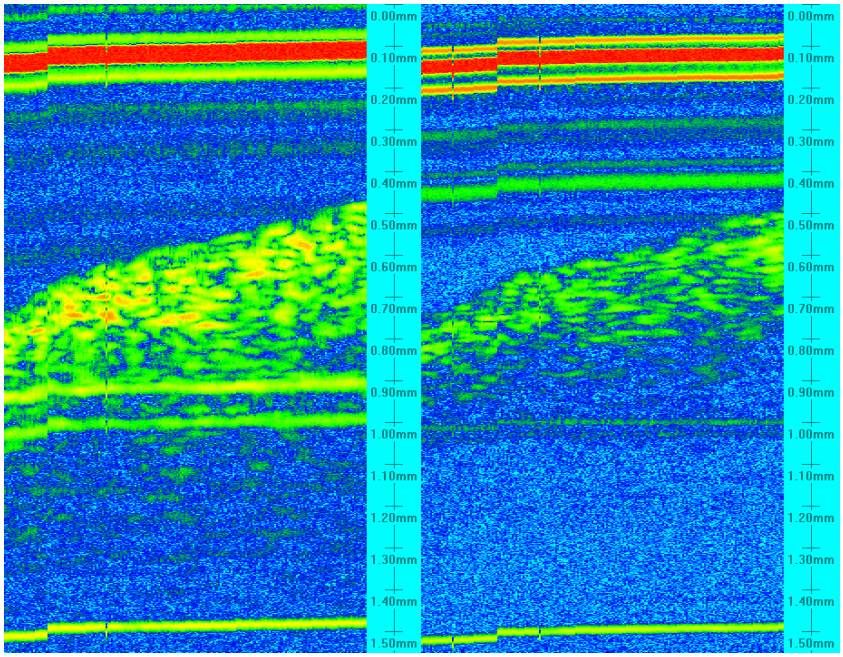

Figure 38. Comparison between two OCT images. Left: Image recorded using the 1300nm AFC source. Right: Image recorded using the 1545nm Superlum source.

applicable here, but again the depth imaged seems to be somewhat larger in the 1300nm system.

6 Conclusion

3 different light sources have been examined for use in OCT imaging: a commercial 1.3μm and a commercial 1.5μm source were compared, and an inexpensive 1.5μm source from the company Giga was also examined. The spectra of the two 1.5μm light sources were measured and Fourier transformed. This showed that the Giga SLD could have promising uses in OCT, as long as attention is payed to the possible problems of the side lobes. It was also seen that the Superlum SLD should be very useful in OCT, since it should offer $\sim$10μm resolution and the side lobes are practically non-existent.

A 1.5μm OCT system was built in both an unbalanced and a balanced setup. This system was used for measuring signal and noise as a function of the mean photocurrent in the detector when using mirrors in both the reference and sample arms. These data were then used to construct a model for estimating the SNR for any choice of system parameters, such as the reflectivity of the sample or the reference. It was seen that this model gives a SNR estimation closer to the experimentally measured SNR, than if the noise had only been calculated theoretically. This model was used for finding the optimal coupler split ratios and optimal reference reflectivity for different system parameters, e.g. it was shown that for low input noise current in the receiver, attenuation of the reference would improve the SNR in unbalanced systems. However, the experimental model suggested that attenuation would not improve the SNR with the system at hand. For balanced systems it was shown that coupler split ratios of 50/50 are not optimal in most cases; using a 25/75 coupler split ratio instead could improve the SNR when 20dB amplification of the measured signal is used (this should also be applicable for

greater amplification, say $40dB$).

The noise measurements also revealed a large amount of $50Hz$ noise, apparently picked up somewhere after filtering. It was seen that this $50Hz$ noise was the dominant noise for low intensities, when no amplification of the measured signal was used. However, it was seen that setting the amplifier to $20dB$ was sufficient to overcome this limitation and allow the shot and beat noise to become dominant at low intensities.

Finally, the system was used for OCT imaging of different samples, using the $1.3\mu m$ source and the Superlum $1.5\mu m$ SLD. Although use of a $1.5\mu m$ source should allow deeper penetration into the examined medium due to less scattering at greater wavelengths, this was not observed when using the mouse biopsy as a sample. This could be explaned if e.g. the collimator was placed slightly worse with respect to the lens, when changing the collimator for using the $1.5\mu m$ source for imaging. The two sources were also used on the same artery biopsy. For the artery biopsy the images were obtained at the same locations in the sample, but this could only be done by using the $1.3\mu m$ fiber system for both the $1.3\mu m$ source and the $1.5\mu m$ source, and this may have caused greater energy losses in the system when using the $1.5\mu m$ source. The biopsy images can therefore not be used directly for comparing the penetration depth.

6.1 Prospects

It was shown that the SNR should improve when e.g. a 25/75 coupler split ratio is used in a balanced setup. This would be interesting to confirm experimentally. Further comparisons of the $1.3\mu m$ and the $1.5\mu m$ penetration depths could also be made, since the measurements at hand were not conclusive. The experimental measurements and modelling could also be done on a balanced system with 3 couplers.

Although the post-filtering $50Hz$ noise is not really a problem when sufficient amplification of the measured signal is used, efforts should be made to find the cause and eliminate it; e.g. it could be examined if the system is sufficiently grounded to a single point.

Additionally, measurements with an alternative low-noise amplifier could be employed, to test whether the $50Hz$ noise was added at the output of the filter. Such a special-built amplifier was readily available in the lab, but further measurements were outside the timeframe of the project.

Acknowledgements

The authors gratefully acknowledge the kind help and support of the inspirating and enthusiastic supervisors of the project:

Peter E. Andersen, Senior scientist, Risø National Laboratory
Andreas Tycho, Ph.D. student, COM, Technical University of Dermark
Anders Bjarklev, Professor, COM, Technical University of Denmark

We would also like to express our sincere gratitude to Lars Thrane, Post Doc., Risø National Laboratory, for helping us with the OCT lab system, and his patience regarding all our questions.
Furthermore, we thank Martin Løbel, Giga ApS, for designing, producing and mounting the $1500nm$ SLD. Finally, we thank Peter S. Jensen for helping us with LaTeX, the staff at the Risø canteen for providing us with an onion, and everyone at the Optics and Fluid Dynamics Department at Risø for providing a good and friendly working atmosphere.

Appendix

A Additional plots

The plot in figure 39 shows the theoretically calculated SNR for an unbalanced system, as a function of the reflectivity R and the receiver input noise current (INC).

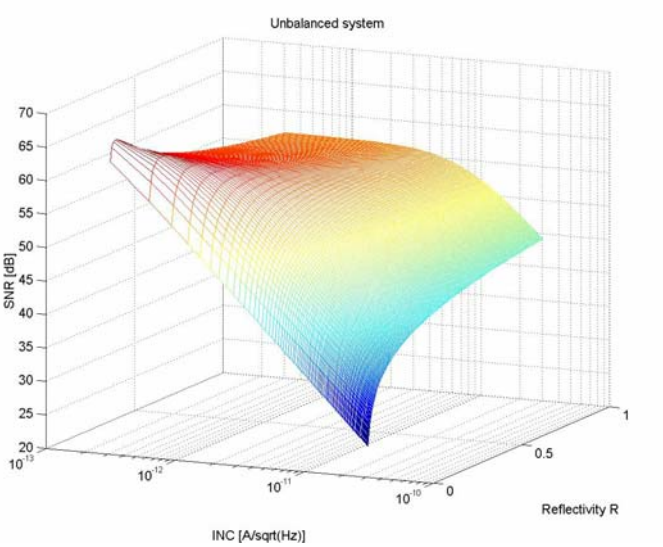

Figure 39. SNR versus the reflectivity and input noise current for an unbalanced system. P_{so} is set to $1mW$, $\Gamma_s = 0.0001$, $\Gamma_x = 0.01$, and the coupler split ratio K is set to $1/2$.

It is seen that for a high INC ($\sim 10^{-10} pA/\sqrt{Hz}$), the reflectivity should be as large as possible, but for a low INC ($\sim 10^{-12} pA/\sqrt{Hz}$) the reference should be attenuated to achieve a SNR improvement.

Figure 40 shows a plot of the estimated SNR as a function of the reflectivity R and the source power P_{so}, using the experimental model for the unbalanced system. It is seen that an attenuation of the reference mirror would not have improved the SNR, under the given system conditions. The maximum source power in figure 40 is $0.5mW$, since it was found that further increasing the power would give a greater I_{dc} than measured experimentally, and thus require extrapolation beyond the datapoints, as mentioned in the report. An amplification of the measured signal might improve the system conditions such that attenuation of the reference would further improve the SNR, as suggested by figure 26.

The plot in figure 41 is a linear version of the one in figure 23, where both the theoretical model and the experimental measurements are seen. The parabolic shape of the curves is clearly seen, although the plot for the experimental measurements with the signal amplified by $20dB$ dominates the visible area of the plot, which makes a comparison difficult.

In figure 23 a series of plots of the noise as a function of the mean photocurrent I_{dc} is shown at different amplifications. These plots cover a system without an attenuator, whereas the plots in figure 42 cover a system with an attenuator. Again the noise level is seen to be slightly lower, for high values of the mean photocurrent, than for the same system without an attenuator.

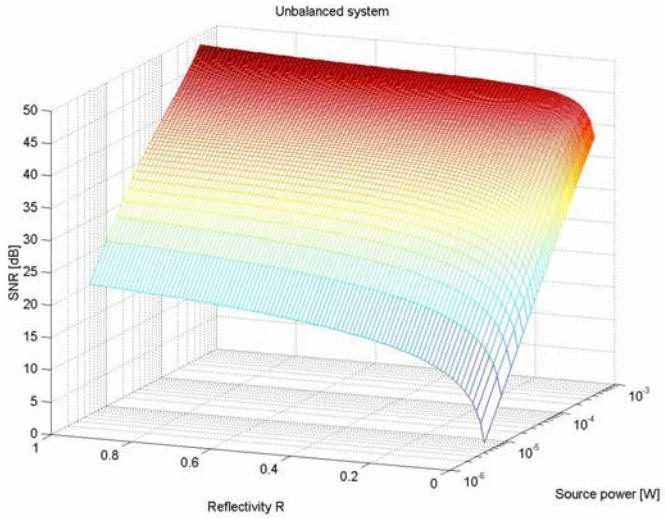

Figure 40. This plot shows the estimated SNR as a function of the reflectivity R and the source power P_{so}, using the experimental model. P_{so} is varied from $5{\cdot}10^{-6}W$ to $5{\cdot}10^{-4}W$. The coupler split ratio K is set to $1/2$, $\Gamma_s = 0.0001$ and $\Gamma_x = 0.01$.

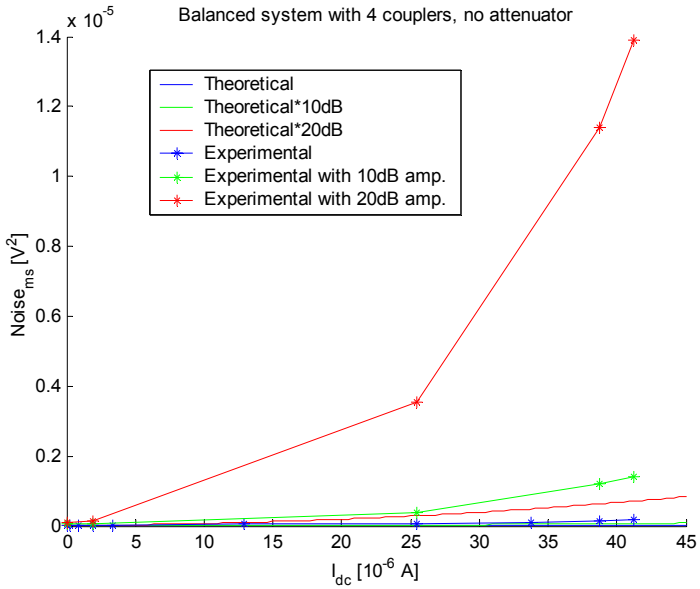

Figure 41. Noise versus dc photocurrent for a balanced system. One plot uses the theoretical model. Three plots based on experimental measurement, for different amplifications. For the theoretical plot, an INC of $3pA/\sqrt{Hz}$ has been assumed.

Figure 43 shows the SNR as a function of the coupler split ratio K_1 and the reflectivity R, for the balanced system with 4 couplers, without an attenuator, using the theoretical model. It is seen that attenuation of the reference would only degrade the SNR, but choosing a split ratio different from 50/50 could improve the SNR. In the unbalanced setup, directing more light towards the sample would mean that more light was also directed back to the source and thereby lost. In the balanced setup however, more light can be be directed towards the sample, without more light being fed back to the source. Including the fact that intensity noise is suppressed in balanced detection and that $\Gamma_s, \Gamma_x \ll R$, these properties

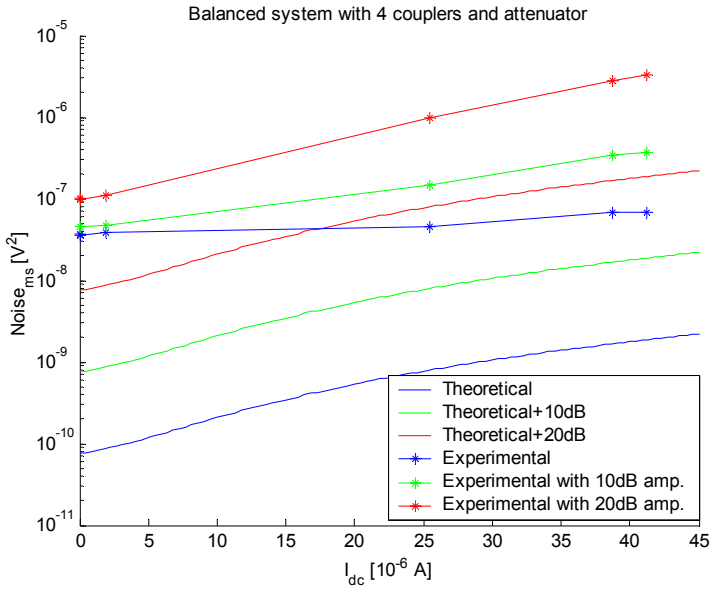

Figure 42. For the theoretical plot, an INC of $3pA/\sqrt{Hz}$ has been assumed.

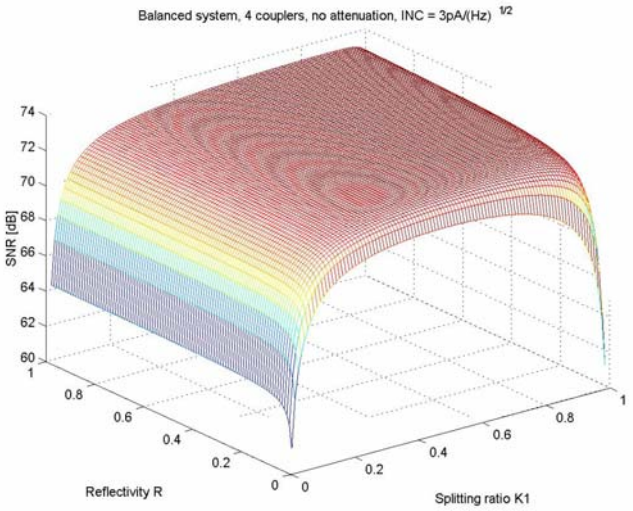

Figure 43. A plot of the estimated SNR versus the coupler split ratio $K1$ and the reflectivity R, for the balanced system with 4 couplers, without an attenuator, using the theoretical model. The source power P_{so} was set to $1mW$, $\Gamma_s = 0.0001$, $\Gamma_x = 0.01$, $K2 = K3 = 1/2$, and an INC value of $3pA/\sqrt{Hz}$ was assumed. The maximum $SNR = 73.3dB$ is obtained when R is maximized and $K1 = 0.87$.

ensure that attenuation of the reference is not necessary, and that directing more light towards the sample is advantageous.

Figures 44, 45 and 46 show the SNR as a function of the reflectivity and the splitting ratio for 0, 10 and $20dB$ amplification, respectively. The experimental model is used. It is seen, when comparing the three figures, that the optimal splitting ratio K_1 increases with the amplification.

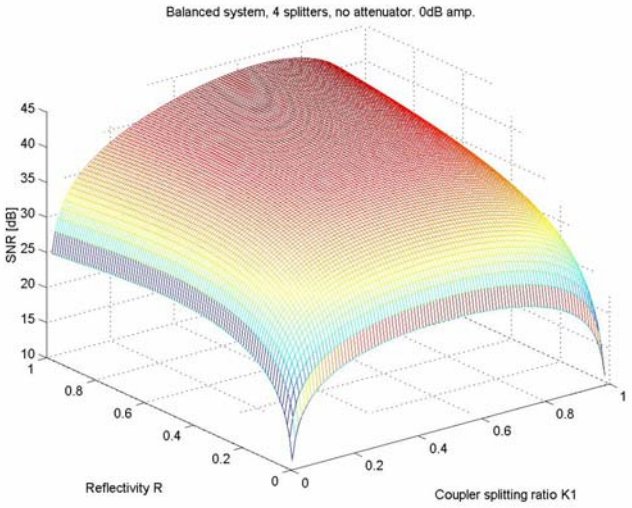

Figure 44. SNR versus reflectivity R and splitting ratio, K_1. The experimental model is used. P_{so} is set to $0.3mW$, $\Gamma_s = 0.0001$, $\Gamma_x = 0.01$, and the coupler split ratios K_2 and K_3 are set to $1/2$. The optimal split ratio K_1 is 0.65 with maximized R giving a $SNR = 44dB$.

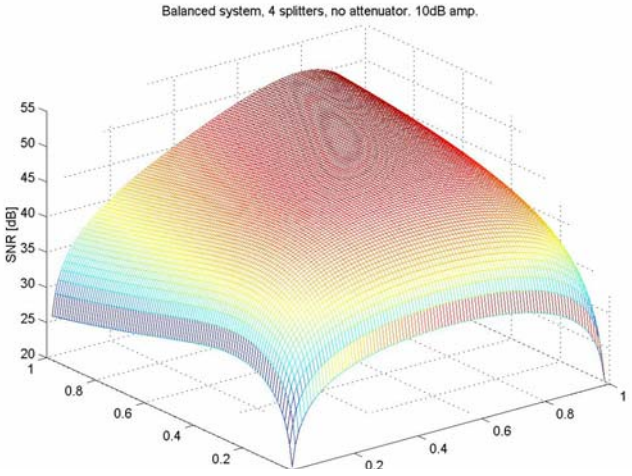

Figure 45. SNR versus reflectivity R and splitting ratio, K_1. The experimental model is used. P_{so} is set to $0.3mW$, $\Gamma_s = 0.0001$, $\Gamma_x = 0.01$, and the coupler split ratios K_2 and K_3 are set to $1/2$. The optimal split ratio K_1 is 0.79 with maximized R giving a $SNR = 51dB$.

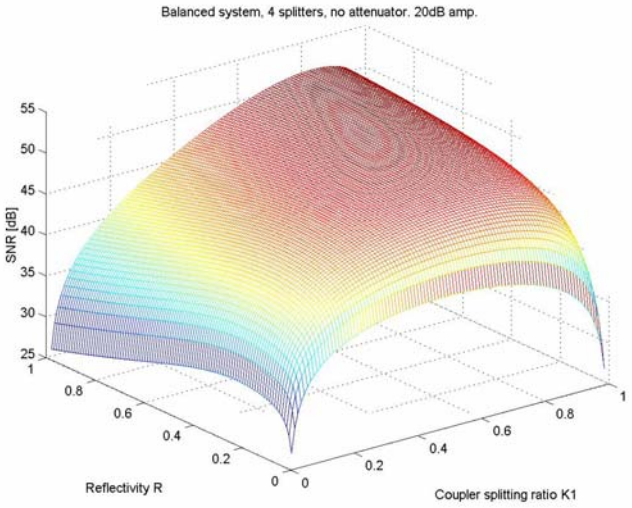

Figure 46. SNR versus reflectivity R and splitting ratio, K_1, using the experimental mode.. P_{so} is set to $0.3mW$, $\Gamma_s = 0.0001$, $\Gamma_x = 0.01$, and the coupler split ratios K_2 and K_3 are set to $1/2$. The optimal split ratio K_1 is 0.83 with maximized R giving a $SNR = 51dB$.

B Calculated conversion factors

These conversion factors were found experimentally as described in section 5.2 and used in the experimental model.

Unbalanced	$0.0824{\cdot}10^6 V/A$
Balanced, without attenuator, $0dB$ amplification	$0.0467{\cdot}10^6 V/A$
Balanced, without attenuator, $10dB$ amplification	$0.149{\cdot}10^6 V/A$
Balanced, without attenuator, $20dB$ amplification	$0.471{\cdot}10^6 V/A$
Balanced, with attenuator, $0dB$ amplification	$0.0290{\cdot}10^6 V/A$
Balanced, with attenuator, $10dB$ amplification	$0.0917{\cdot}10^6 V/A$
Balanced, with attenuator, $20dB$ amplification	$0.290{\cdot}10^6 V/A$

C Matlab code used for the experimental model

Only the code used for the balanced system with an attenuator is shown, as the code used for the unbalanced system and the balanced system without attenuator is very similar.

noiseplot_Idc.m:

```
% Balanced, 4 splitters, 4.5dB attenuator (datafiles: w3dBwcut.xls,
% w3dBwcut_10dBfilter.xls, w3dBwcut_20dBfilter.xls)
% Plots the theoretical and the experimentally measured noise (V_ms)
% as a function of I_dc.

clear
% System parameters

% FWHM wavelength bandwidth of the source
delta_lambda = 62 * 10^-9; % 62nm measured for the SuperLum source

% Optical bandwidth of the source
delta_nu=sqrt(pi/(2*log(2)))*3*10^8*delta_lambda/(1545*10^-9)^2;

% Electric detection bandwidth
b = 10*10^3;

% Polarisation coefficient. 0 for unpolarized, 1 for polarized
v = 0;

% The noise was measured for I_dc varying from 0 to 45muA
I_dc = linspace(0,45,100);
% In the experiments two mirrors were used and only 50/50 couplers,
% so I_r = I_x = 1/2 * I_dc
I_r = 0.5 * I_dc;
I_x = I_r;

for i =1:100
   % The factor 0.029 V/A is the estimated impedance,
```

```
   % converting the theoretical current into voltage
   noise_theor(i) = (0.029E6)^2 *
                noise_of_Idc_theoretical(I_r(i)*1E-6,I_x(i)*1E-6,b,delta_nu,v);
end

% The experimentally determined noise, pointwise
I_dc_point = [0 0.034 1.876 25.46 38.69 41.21];

noise_exper_point = [3.69E-08 3.53E-08 3.94E-08 4.59E-08 6.71E-08 6.93E-08];
noise_exper_point_10dB = [4.55E-08 4.48E-08 4.73E-08 1.47E-07 3.46E-07 3.69E-07];
noise_exper_point_20dB = [1.01E-07 1.00E-07 1.12E-07 9.89E-07 2.81E-06 3.35E-06];

hold on
plot(I_dc,noise_theor,'b', I_dc,10*noise_theor,'g', I_dc,10^2*noise_theor,'r')
plot(I_dc_point,noise_exper_point,'b*-')
plot(I_dc_point,noise_exper_point_10dB,'g*-')
plot(I_dc_point,noise_exper_point_20dB,'r*-')

xlabel('I_d_c [10^-^6 A]'), ylabel('Noise_m_s [V^2]'),
        title('Balanced system with 4 couplers and attenuator')
legend('Theoretical','Theoretical+10dB','Theoretical+20dB',
       'Experimental','Experimental with 10dB amp.','Experimental with 20dB amp.')
hold off
```

find_fit.m:

```
% Makes fit to experimental data

clear

I_dc_point = [0 0.0453666 2.441153 33.22953 50.61081 53.8827];
noise_exper_point = [1.01E-07 1.00E-07 1.12E-07 9.89E-07 2.81E-06 3.35E-06];

parameters = nlinfit(I_dc_point,noise_exper_point,'third_order_polyn',
            [1E-10 1E-10 1E-10 3E-8])

a = parameters(1);
b = parameters(2);
c = parameters(3);
d = parameters(4);
%e = parameters(5);

I_dc = linspace(0,55,100);
noise_fitted = a*I_dc.^3 + b*I_dc.^2 + c*I_dc + d;

plot(I_dc,noise_fitted,I_dc_point,noise_exper_point,'*-')
xlabel('I_d_c [10^-^6 A]'), ylabel('Noise_m_s [V^2]')
title('Balanced system, 4 splitters, with attenuator')
legend('Fit to data','Experimental data')
```

third_order_polyn.m:

```
% Model used by find_fit.m. Fits to a 3rd order polynomial
```

```
function [P] = third_order_polyn(parameters,I_dc)

a = parameters(1);
b = parameters(2);
c = parameters(3);
d = parameters(4);

P = a*I_dc.^3 + b*I_dc.^2 + c*I_dc + d;
```

noise_of_Idc_theoretical.m:

```
% Balanced detection with 4 couplers and a 4.5dB attenuator (0.353)
% Calculates theoretical noise (mean-square) contributions as a function of I_dc

function [noise] = noise_of_Idc_theoretical(I_r,I_x,b,delta_nu,v)

% 4,5 dB attenuator, 1545nm
d = 0.353;

sigma_re = (3*10^-12)^2 * b;
sigma_sh = 2 * (1+d) * 1.6*10^-19 * (I_r+I_x) * b;
sigma_be = (1+d) * 4 *(1+v^2) * I_r * I_x * b/delta_nu;

noise = sigma_re + sigma_sh + sigma_be;
```

snrplot_vs_Idc_2D.m:

```
% Balanced detection, 4 splitters, with 4.5dB attenuation (a 3dB 1300nm attenuator)
% Plots the SNR as a function of the I_dc in 3 ways:
% 1) Theoretically
% 2) Theoretically calculated I_s but experimentally measured noise
% 3) Experimentally
% Datafiles used: Balanced noise_w3dBwcut.xls, Balanced noise_w3dBwcut_10dBfilter.xls
% og Balanced noise_w3dBwcut_20dBfilter.xls

clear
% System parameters

% 4.5dB attenuation
att = 0.353;

% Parameters used to fit to 3rd order polynomial. Found using find_fit.m
a_0dB = 3.9200e-013;
b_0dB = -1.7980e-011;
c_0dB = 4.6348e-010;
d_0dB = 3.6766e-008;

a_10dB = 2.6629e-012;
b_10dB = -9.1704e-011;
c_10dB = 3.4691e-009;
d_10dB = 4.3593e-008;

a_20dB = 2.0228e-011;
b_20dB = -1.3955e-010;
```

```
c_20dB = 9.0289e-009;
d_20dB = 9.7388e-008;

% The SNR is plotted for values of P_so from P_so_init to 100*P_so_init
P_so_init =5.4E-6;

% Detector responsivity [A/W]
rho = 1;

% Perhaps this is not optimal, but was used in the experiments
K1 = 0.5;
K2 = 0.5;
K3 = 0.5;

% Reflection coefficients, estimated for two mirrors
gamma_s = 0.6;
gamma_x = 0.6;
R = 0.6;

% FWHM wavelength bandwidth of the source
delta_lambda = 62 * 10^-9; % 62nm measured for the SuperLum source

% Optical bandwidth of the source
delta_nu=sqrt(pi/(2*log(2)))*3*10^8*delta_lambda/(1545*10^-9)^2;

% Electric detection bandwidth
B = 10*10^3;

% Polarisation coefficient. 0 for unploarized, 1 for polarized
v = 0;

% The receiver noise is set to the noise equivalent power, NEP
NEP = 3E-12;

for P_so = 1:100
   P_r = 1/2 * P_so * P_so_init * (1-K1) * K3 * (1-K3) * R;
   P_s = 1/2 * P_so * P_so_init * K1 * K2 * (1-K2) * gamma_s;
   P_x = 1/2 * P_so * P_so_init * K1 * K2 * (1-K2) * gamma_x;
   % 0.0824E6 is the estimated impedance, converting current to voltage
   V2_s_theor(P_so) = (0.0467E6)^2 * ((1+att)*2)^2 * rho^2 * P_r * P_s;
   I_s_theor(P_so) = ((1+att)*2)^2 * rho^2 * P_r * P_s;
   I_dc(P_so) = (1+att)*rho*(P_r + P_x);
   if I_dc(P_so) > 55E-6
      I_dc(P_so)
      P_so
      error('I_dc larger than 55muA. There are no experimental data
for this parameter domain. Turn source power P_so down.')
   end
   sigma2_v_exper_0dB(P_so) = a_0dB*(I_dc(P_so)*1E6)^3 +
 b_0dB*(I_dc(P_so)*1E6)^2 + c_0dB*(I_dc(P_so)*1E6) + d_0dB;
   SNR_exper_noise_0dB(P_so) = 10*log10(V2_s_theor(P_so) / sigma2_v_exper_0dB(P_so));

   sigma2_v_exper_10dB(P_so) = a_10dB*(I_dc(P_so)*1E6)^3 +
 b_10dB*(I_dc(P_so)*1E6)^2 + c_10dB*(I_dc(P_so)*1E6) + d_10dB;
```

```
   SNR_exper_noise_10dB(P_so) = 10*log10(10*V2_s_theor(P_so) / sigma2_v_exper_10dB(P_so));

   sigma2_v_exper_20dB(P_so) = a_20dB*(I_dc(P_so)*1E6)^3 +
 b_20dB*(I_dc(P_so)*1E6)^2 + c_20dB*(I_dc(P_so)*1E6) + d_20dB;
   SNR_exper_noise_20dB(P_so) = 10*log10(10^2*V2_s_theor(P_so) / sigma2_v_exper_20dB(P_so));

   sigma2_i_theor(P_so) = 2*1.6E-19*I_dc(P_so)*B +
 2*(1+att)^2*(1+v^2)*rho^2*P_r*P_x*B/delta_nu + NEP^2*B;
   SNR_theor(P_so) = 10*log10(I_s_theor(P_so) / sigma2_i_theor(P_so));
end

I_dc_exper = 1E-6 * [2.441153 33.22953 50.61081 53.8827];
I_dc_exper_10dB = 1E-6 * [0.0453666 2.441153 33.22953 50.61081 53.8827];
SNR_exper_0dB = [51.83038618 73.16426167 75.03661936 75.44912458];
SNR_exper_10dB = [23.6102406 61.0370322 78.11250528 77.91250457 78.18693809];
SNR_exper_20dB = [29.10487751 67.30088477 79.82658616 78.8178954 78.59714325];

hold on
plot(I_dc,SNR_theor,'k')
plot(I_dc,SNR_exper_noise_0dB,'b')
plot(I_dc_exper,SNR_exper_0dB,'b*')
plot(I_dc,SNR_exper_noise_10dB,'g')
plot(I_dc_exper_10dB,SNR_exper_10dB,'g*')
plot(I_dc,SNR_exper_noise_20dB,'r')
plot(I_dc_exper_10dB,SNR_exper_20dB,'r*')

hold off

xlabel('Mean photocurrent I_d_c [A]'), ylabel('SNR [dB]')
title('Balanced system, 4 couplers, with attenuator')
legend('Purely theoretical', 'Theoretical signal,experimental noise (0dB amp.)',
 'Purely experimental (0dB amp.)','Theoretical signal, experimental noise (10dB amp.)',
 'Purely experimental (10dB amp.)','Theoretical signal, experimental noise (20dB amp.)',
 'Purely experimental (20dB amp.)')
```

snrplot_vs_K1_amp_EXPER_2D.m:

```
% Balanced detection, 4 splitters, with attenuator
% Plots the SNR as a function of coupler splitting ratio K1 and the amplification.
% Uses fitted EXPERIMENTAL data to estimate the noise, but the theoretical model
% to estimate the signal.

clear
% System parameters

% 4.5dB attenuation
att = 0.353;

% Parameters used to fit to 3rd order polynomial. Found using find_fit.m
a_0dB = 3.9200e-013;
b_0dB = -1.7980e-011;
c_0dB = 4.6348e-010;
d_0dB = 3.6766e-008;
```

```
a_10dB = 2.6629e-012;
b_10dB = -9.1704e-011;
c_10dB = 3.4691e-009;
d_10dB = 4.3593e-008;

a_20dB = 2.0228e-011;
b_20dB = -1.3955e-010;
c_20dB = 9.0289e-009;
d_20dB = 9.7388e-008;

% Source power [W]
P_so =4E-4;

% Detector responsivity [A/W]
rho = 1;

% Reflection coefficients
gamma_s = 0.0001;
gamma_x = 0.01;
R = 0.7;

% This is always optimal
K2 = 0.5;
K3 = 0.5;

% FWHM wavelength bandwidth of the source
delta_lambda = 62 * 10^-9; % 62nm measured for the SuperLum source

% Optical bandwidth of the source
delta_nu=sqrt(pi/(2*log(2)))*3*10^8*delta_lambda/(1545*10^-9)^2;

% Polarisation coefficient. 0 for unpolarized, 1 for polarized
v = 0;

for K1 = 1:99
   P_r = 1/2 * P_so * (1-K1/100) * K3 * (1-K3) * R;
 P_s = 1/2 * P_so * K1/100 * K2 * (1-K2) * gamma_s;
   P_x = 1/2 * P_so * K1/100 * K2 * (1-K2) * gamma_x;
   % 0.0467E6 is the estimated impedance, converting current to voltage
   V2_s(K1) = (0.0467E6)^2 * (2*(1+att))^2 * rho^2 * P_r * P_s;
   I_dc = (1+att)*rho*(P_r + P_x);
   if I_dc > 55E-6
      I_dc
      error('I_dc larger than 55muA. There are no experimental data
 for this parameter domain. Turn source power P_so down.')
   end
   sigma2_v_exper_0dB(K1) = a_0dB*(I_dc*1E6)^3 + b_0dB*(I_dc*1E6)^2 +
      c_0dB*(I_dc*1E6) + d_0dB;
   SNR_exper_noise_0dB(K1) = 10*log10(V2_s(K1) / sigma2_v_exper_0dB(K1));

   sigma2_v_exper_10dB(K1) = a_10dB*(I_dc*1E6)^3 + b_10dB*(I_dc*1E6)^2 +
      c_10dB*(I_dc*1E6) + d_10dB;
   SNR_exper_noise_10dB(K1) = 10*log10(10*V2_s(K1) / sigma2_v_exper_10dB(K1));
```

```
   sigma2_v_exper_20dB(K1) = a_20dB*(I_dc*1E6)^3 +
      b_20dB*(I_dc*1E6)^2 + c_20dB*(I_dc*1E6) + d_20dB;
   SNR_exper_noise_20dB(K1) = 10*log10(10^2*V2_s(K1) / sigma2_v_exper_20dB(K1));
end

[SNRmax_0dB K1_opt_0dB] = max(SNR_exper_noise_0dB);
SNRmax_0dB
K1_opt_0dB

[SNRmax_10dB K1_opt_10dB] = max(SNR_exper_noise_10dB);
SNRmax_10dB
K1_opt_10dB

[SNRmax_20dB K1_opt_20dB] = max(SNR_exper_noise_20dB);
SNRmax_20dB
K1_opt_20dB

K1 = linspace(0.01,0.99,99);

hold on
plot(K1,SNR_exper_noise_0dB,'b')
plot(K1,SNR_exper_noise_10dB,'g')
plot(K1,SNR_exper_noise_20dB,'r')
hold off

xlabel('Coupler splitting ratio K1'), ylabel('SNR [dB]')
title('Balanced system, 4 splitters, with attenuator')
legend('0dB amp.','10dB amp.','20dB amp.')
```

snrplot_vs_K1_sigma_re_THEOR_2D.m:

```
% Balanced detection, 4 splitters, with attenuator
% Plots the SNR as a function of the reflectivity R of the reference mirror
% and the coupler splitting ratio K1 in 2D.
% THEORETICAL MODEL

clear
% System parameters

% 4.5dB attenuation
att = 0.353;

% Detector responsivity [A/W]
rho = 1;

% Source power [W]
P_so = 1*10E-3;

% The SNR vs. R and K plot in 3D showed that R should always be maximized
R = 0.9;

% The optimal splitting ratio K1 is determined by sigma_re
       approximated by the NEP [A/sqrt(Hz)]
NEP = [3E-13 3E-12 3E-11];
```

```
% Reflection coefficients
gamma_s = 0.0001;
gamma_x = 0.01;
% 50/50 couplers are always optimal for K2 and K3
K2 = 0.5;
K3 = 0.5;

% FWHM wavelength bandwidth of the source
delta_lambda = 62 * 10^-9; % 62nm measured for the SuperLum source

% Optical bandwidth of the source
delta_nu=sqrt(pi/(2*log(2)))*3*10^8*delta_lambda/(1545*10^-9)^2;

% Electric detection bandwidth [Hz]
b = 10*10^3;

% Polarisation coefficient. 0 for unpolarized, 1 for polarized
v = 0;

for K1 = 1:99
   P_r = 1/2 * P_so * (1-K1/100) * K3 * (1-K3) * R;
   P_s = 1/2 * P_so * K1/100 * K2 * (1-K2) * gamma_s;
   P_x = 1/2 * P_so * K1/100 * K2 * (1-K2) * gamma_x;
   I_s(K1) = ((1+att)*2)^2 * rho^2 * P_r * P_s;
   I_dc = (1+att)*rho*(P_r+P_x);
   sigma2_i(K1,:) = 2*1.6E-19*I_dc*b +
      2*(1+att)^2*(1+v^2)*rho^2*P_r*P_x*b/delta_nu + NEP.^2*b;
   SNR(K1,:) = 10*log10(I_s(K1) ./ sigma2_i(K1,:));
end

K1 = linspace(0.01,0.99,99);
[SNRmax K1_opt] = max(max(SNR'));
SNRmax
K1_opt

hold on
plot(K1,SNR(:,1),'b')
plot(K1,SNR(:,2),'g')
plot(K1,SNR(:,3),'r')
hold off

xlabel('Splitting ratio K1'), ylabel('SNR [dB]')
title('Balanced system, 4 couplers, with attenuation')
legend('INC = 3*10^-^1^3 A/(Hz)^-^1^2','INC = 3*10^-^1^2 A/(Hz)^-^1^2',
     'INC = 3*10^-^1^1 A/(Hz)^-^1^2')
```

snrplot_vs_R_and_K_THEOR_3D.m:

```
% Balanced detection, 4 splitters, with attenuator
% Plots the SNR as a function of the reflectivity R of the reference mirror
% and the coupler splitting ratio K1 in 3D.
% THEORETICAL MODEL
```

```
clear
% System parameters

% 4.5dB attenuation
att = 0.353;

% Detector responsivity [A/W]
rho = 1;

% Source power [W]
P_so = 1*10E-3;

% The receiver noise is approximated as the noise equivalent power, NEP [A/sqrt(Hz)]
NEP = 3E-12;

% Reflection coefficients
gamma_s = 0.0001;
gamma_x = 0.01;
% 50/50 couplers are always optimal for K2 and K3
K2 = 0.5;
K3 = 0.5;

% FWHM wavelength bandwidth of the source
delta_lambda = 62 * 10^-9; % 62nm measured for the SuperLum source

% Optical bandwidth of the source
delta_nu=sqrt(pi/(2*log(2)))*3*10^8*delta_lambda/(1545*10^-9)^2;

% Electric detection bandwidth
b = 10*10^3;

% Polarisation coefficient. 0 for unploarized, 1 for polarized
v = 0;

for R =1:99
   for K1 = 1:99
      P_r = 1/2 * P_so * (1-K1/100) * K3 * (1-K3) * R/100;
      P_s = 1/2 * P_so * K1/100 * K2 * (1-K2) * gamma_s;
      P_x = 1/2 * P_so * K1/100 * K2 * (1-K2) * gamma_x;
      I_s(R,K1) = ((1+att)*2)^2 * rho^2 * P_r * P_s;
      I_dc = (1+att)*rho*(P_r+P_x);
      sigma2_i(R,K1) = 2*1.6E-19*I_dc*b +
       2*(1+att)^2*(1+v^2)*rho^2*P_r*P_x*b/delta_nu + NEP^2*b;
      SNR(R,K1) = 10*log10(I_s(R,K1) / sigma2_i(R,K1));
   end
end

R = linspace(0.01,0.99,99);
K = linspace(0.01,0.99,99);
[SNRmax K1_opt] = max(max(SNR));
[SNRmax R_opt] = max(max(SNR'));
SNRmax
K1_opt
R_opt
```

```
mesh(K,R,SNR)
xlabel('Splitting ratio K1'), ylabel('Reflectivity R'),zlabel('SNR [dB]')
title('Balanced system, 4 couplers, with attenuation, INC=3pA/(Hz)^-^1^/^2')
```

snrplot_vs_R_and_K1_EXPER_3D.m:

```
% Balanced detection, 4 splitters, with attenuator
% Plots the SNR as a function of the reflectivity R of the reference mirror,
% and the coupler splitting ratio K1.
% Uses fitted EXPERIMENTAL data to estimate the noise, but the theoretical model
% to estimate the signal.

clear
% System parameters

% 4.5dB attenuation
att = 0.353;

% Parameters used to fit to 3rd order polynomial. Found using find_fit.m
a_0dB = 3.9200e-013;
b_0dB = -1.7980e-011;
c_0dB = 4.6348e-010;
d_0dB = 3.6766e-008;

a_10dB = 2.6629e-012;
b_10dB = -9.1704e-011;
c_10dB = 3.4691e-009;
d_10dB = 4.3593e-008;

a_20dB = 2.0228e-011;
b_20dB = -1.3955e-010;
c_20dB = 9.0289e-009;
d_20dB = 9.7388e-008;

% Source power [W]. THE NATURE OF THIS PLOT DEPENDS MUCH ON THIS PARAMETER
P_so =3E-4;

% Detector responsivity [A/W]
rho = 1;

% Reflection coefficients
gamma_s = 0.0001;
gamma_x = 0.01;

% This is always optimal
K2 = 0.5;
K3 = 0.5;

% FWHM wavelength bandwidth of the source
delta_lambda = 62 * 10^-9; % 62nm measured for the SuperLum source

% Optical bandwidth of the source
delta_nu=sqrt(pi/(2*log(2)))*3*10^8*delta_lambda/(1545*10^-9)^2;
```

```
% Polarisation coefficient. 0 for unploarized, 1 for polarized
v = 0;

for R =1:99
   for K1 = 1:99
      P_r = 1/2 * P_so * (1-K1/100) * K3 * (1-K3) * R/100;
    P_s = 1/2 * P_so * K1/100 * K2 * (1-K2) * gamma_s;
    P_x = 1/2 * P_so * K1/100 * K2 * (1-K2) * gamma_x;
      % 0.029E6 is the estimated impedance, converting current to voltage
      V2_s(R,K1) = (0.029E6)^2 * ((1+att)*2)^2 * rho^2 * P_r * P_s;
      I_dc = (1+att)*rho*(P_r + P_x);
      if I_dc > 55E-6
         I_dc
         error('I_dc larger than 55muA. There are no experimental
      data for this parameter domain. Turn source power P_so down.')
      end
      sigma2_v_exper_0dB(R,K1) = a_0dB*(I_dc*1E6)^3 +
      b_0dB*(I_dc*1E6)^2 + c_0dB*(I_dc*1E6) + d_0dB;
    SNR_exper_noise_0dB(R,K1) = 10*log10(V2_s(R,K1) / sigma2_v_exper_0dB(R,K1));

    sigma2_v_exper_10dB(R,K1) = a_10dB*(I_dc*1E6)^3 +
      b_10dB*(I_dc*1E6)^2 + c_10dB*(I_dc*1E6) + d_10dB;
    SNR_exper_noise_10dB(R,K1) = 10*log10(10*V2_s(R,K1) / sigma2_v_exper_10dB(R,K1));

    sigma2_v_exper_20dB(R,K1) = a_20dB*(I_dc*1E6)^3 +
      b_20dB*(I_dc*1E6)^2 + c_20dB*(I_dc*1E6) + d_20dB;
    SNR_exper_noise_20dB(R,K1) = 10*log10(10^2*V2_s(R,K1) / sigma2_v_exper_20dB(R,K1));
   end
end

[SNRmax_0dB K1_opt_0dB] = max(max(SNR_exper_noise_0dB));
[SNRmax_0dB R_opt_0dB] = max(max(SNR_exper_noise_0dB'));
SNRmax_0dB
K1_opt_0dB
R_opt_0dB

[SNRmax_10dB K1_opt_10dB] = max(max(SNR_exper_noise_10dB));
[SNRmax_10dB R_opt_10dB] = max(max(SNR_exper_noise_10dB'));
SNRmax_10dB
K1_opt_10dB
R_opt_10dB

[SNRmax_20dB K1_opt_20dB] = max(max(SNR_exper_noise_20dB));
[SNRmax_20dB R_opt_20dB] = max(max(SNR_exper_noise_20dB'));
SNRmax_20dB
K1_opt_20dB
R_opt_20dB

R = linspace(0.01,0.99,99);
K1 = linspace(0.01,0.99,99);
mesh(K1,R,SNR_exper_noise_0dB)
xlabel('Coupler splitting ratio K1'), ylabel('Reflectivity R')
zlabel('SNR [dB]'),title('Balanced system, 4 splitters, with attenuator. 0dB amp.')
```

```
figure
mesh(K1,R,SNR_exper_noise_10dB)
xlabel('Coupler splitting ratio K1'), ylabel('Reflectivity R')
zlabel('SNR [dB]'),title('Balanced system, 4 splitters, with attenuator. 10dB amp.')

figure
mesh(K1,R,SNR_exper_noise_20dB)
xlabel('Coupler splitting ratio K1'), ylabel('Reflectivity R')
zlabel('SNR [dB]'),title('Balanced system, 4 splitters, with attenuator. 20dB amp.')
```

References

[1] J. G. Fujimoto, W. Drexler, U. Morgner, F. Kärtner, and E. Ippen, Optical Coherence Tomography: High Resolution Imaging Using Echoes of Light, Optics & Photonics News , 25–31 (January 2000).

[2] F. L. Pedrotti and L. S. Pedrotti, *Introduction to Optics*, Prentice-Hall International, Inc., 2. edition, 1996.

[3] J. W. Goodman, *Statistical Optics*, John Wiley & Sons, 1985, ISBN 0-471-01502-4.

[4] E. Saff and A. Snider, *Fundamentals of Complex Analysis for Mathematics, Science and Engineering*, Prentice Hall, 2. edition edition, 1993, ISBN 0-13-327461-6.

[5] J. M. Schmitt, Optical Coherence Tomography (OCT): A Review, IEEE Journal of Selected Topics in Quantum Electronics **5**(4), 1205–1215 (July/August 1999).

[6] B. Saleh and M. Teich, *Fundamentals of Photonics*, John Wiley & Sons, 1991, ISBN 0-471-839-65-5.

[7] L. Thrane, *Optical Coherence Tomography: Modelling and Applications*, PhD thesis, Risø-R-1217(EN), 2000.

[8] H. W. Ott, *Noise Reduction Techniques in Electronic Systems*, John Wiley & Sons, Inc., 2. edition, 1988, ISBN 0-471-85068-3.

[9] K. Conradsen, *En Introduktion Til Statistik*, volume 1A, IMM, DTU, Lyngby, 1999.

[10] A. Rollins and J. A. Izatt, SNR Analysis of Conventional and Optimal Fiber-Optic Low-Coherence Interferometer Topologies, Proceedings of SPIE **3915**, 60–67 (2000).

[11] F. Grum and R. J. Becherer, *Radiometry*, volume 1 of *Optical Radiation Measurements*, Academic Press, 1979, ISBN 0-12-304901 (v. 1).

[12] New Focus, *Nirvana Auto-Balanced Photoreceivers*, Model 2007 & 2017, User's Manual.

[13] K. Takada, Noise in Optical Low-Coherence Reflectrometry, IEEE Journal of Quantum Electronics **34**, 1098–1106 (1998).

[14] A. G. Podoleanu, Unbalanced versus Balanced Operation in an Optical Coherence Tomography System, Appl. Opt. **39**(1), 173–182 (January 2000).

[15] E. A. S. et Al., Optical Coherence Tomography: Principles, Instrumentation, and Biological Applications, in *Biomedical Optical Instrumentation and Laser-Assisted Biotechnology*, edited by A. M. V. S. el Al., pages 291–303, Kluwer Acedemic Publishers, 1996.

[16] U. Haberland, W. Rütten, V. Blazek, and H. J. Schmitt, Investigation of Highly Scattering Media Using Near-Infrared Continuous Wave Tunable Semiconductor Laser, in *Optical Tomography, Photon Migration, and Spectroscopy of Tissue and Model Media: Theory, Human Studies, and Instrumentation*, edited by B. Chance and R. R. Alfano, pages 503–512, Proc. SPIE 2389, February 1995.

[17] L. Thrane, Private communication, June/July 2001.

Bibliographic Data Sheet **Risø–R–1278(EN)**

Title and author(s)

Optical Coherence Tomography: System Design and Noise Analysis

Michael H. Frosz, Michael Juhl and Morten H. Lang

ISBN	ISSN
87-550-2905-1; 87-550-2904-3 (Internet)	0106-2840

Dept. or group	Date
Optics and Fluid Dynamics Department	July 2001

Groups own reg. number(s)	Project/contract No.

Sponsorship

Pages	Tables	Illustrations	References
63	1	46	17

Abstract (Max. 2000 char.)

The basic properties of an Optical Coherence Tomography (OCT) system, such as coherence and interference are presented. A $1.3\mu m$ light source and a $1.5\mu m$ source is examined and used in OCT imaging for comparison of penetration depth. No improvement was shown with the $1.5\mu m$ system, but is expected theoretically. A simple inexpensive $1.5\mu m$ source was also examined for use in OCT, and shows promising results, based on a spectral analysis. Noise in unbalanced and balanced detection is examined theoretically. The noise and SNR is measured experimentally for a given system, showing that the theoretical model does not give a good estimate. A model is therefore constructed using the experimental noise measurements, and shown to give better estimations of the SNR than the theoretical model. Using the new model, it is shown that attenuation of the reference power does not improve the SNR in the examined system when using unbalanced detection, as expected when using the theoretical model. It is also found that using a 25/75 coupler split ratio instead of 50/50 in balanced detection, should improve the SNR. A $50Hz$ noise was found to be picked up after filtering, and is shown to limit the SNR when no amplification of the measured signal is used.

Descriptors INIS/EDB

Available on request from:
Information Service Department, Risø National Laboratory
(Afdelingen for Informationsservice, Forskningscenter Risø)
P.O. Box 49, DK–4000 Roskilde, Denmark
Phone (+45) 46 77 46 77, ext. 4004/4005 · Fax (+45) 46 77 40 13
E-mail: risoe@risoe.dk